https://doi.org/10.5194/essd-2026-278
Preprint. Discussion started: 19 June 2026

Open Access Earth System Science Data Discussions

Machine Learning-Based Fusion of Multi-Source Daily Precipitation Products for the Tibetan Plateau Rainy Season

Zuo Wen[1,2], Baiquan Zhou[1*], Panmao Zhai[1]

[1]State Key Laboratory of Severe Weather, Chinese Academy of Meteorological Sciences, Beijing, 100081, China

[2]Department of Atmospheric and Oceanic Sciences & Institute of Atmospheric Sciences, Fudan University, 200438, Shanghai, China

Correspondence to: Baiquan Zhou (zhoubq@cma.gov.cn)

Abstract. As the "Asian Water Tower," the Tibetan Plateau (TP) critically influences regional water security and global climate. Yet, due to its complex terrain and scarce observations, existing precipitation products poorly represent precipitation characteristics over the western.TP. Here, we present 3DMergePrec (3DM), a 0.25° daily precipitation dataset for the TP rainy seasons (1961–2021), generated by fusing 12 mainstream products using a deep learning framework combining Graph Attention Networks and 3D Convolutional Neural Networks. Validated against long-term observations (CMA stations) and independently verified with automatic stations in the western and central-western TP, 3DM demonstrates robust performance: Overall, it reduces mean squared error by 30–40% compared to satellite-only products (e.g., TRMM, GPM) and effectively mitigates the high-error belt in the southeastern TP. Crucially, in the data-sparse western TP, 3DM achieves RMSE reductions of 25–40% (e.g., mean squared error of 10.78 mm in the Qiangtang region), outperforming existing products. Its long-term precipitation trends closely align with observations, surpassing most counterparts. Limitations include underestimation of extreme precipitation frequency and overestimation of light precipitation days, with limited improvement in precipitation detection—likely due to the lack of dynamical constraints. Overall, 3DM offers stable, spatially continuous, and accurate precipitation estimates, particularly in the western TP, providing a valuable long-term dataset to support climate change studies across the region.

Keywords: Tibetan Plateau, data fusion, multi-source precipitation products, Graph Attention Network, machine learning

1. Introduction

The Tibetan Plateau, with mean elevation exceeding 4,000 meters, is the highest-altitude region over the world and hosts the largest number of glaciers outside the polar regions. Its complex surface conditions exhibit high vulnerability and sensitivity to external perturbations, and has therefore been receiving extensive global attention (Li, G. *et al.*, 2022; Yan,

https://doi.org/10.5194/essd-2026-278
Preprint. Discussion started: 19 June 2026

Open Access Earth System Science Data Discussions

Y. *et al.*, 2020; You *et al.*, 2021). The observed climate warming on the Tibetan Plateau exhibits a pronounced amplification effect compared to global warming. This has accelerated the transition from solid to liquid water, driving glacial retreat, lake expansion, and regional hydrological imbalances. These changes threaten water security in downstream regions and impact ecosystems, as well as agricultural and pastoral livelihoods (Chen, W. *et al.*, 2022; Qiu, 2014; Yao, F. *et al.*, 2018; Yao, T. *et al.*, 2019). The complex terrain and sparse population of the Tibetan Plateau have resulted in long-term climate observations being primarily concentrated in its eastern regions (Miao *et al.*, 2024),. This spatial bias significantly limits our understanding of climate change across the entire region, particularly concerning precipitation change. While numerous gridded precipitation datasets have been generated through interpolation, satellite retrieval, and reanalysis (Beck *et al.*, 2017; Du *et al.*, 2022), their ability to characterize long-term precipitation changes—especially in the western TP—remains highly uncertain due to the inherent limitations of each methodology. The reliability of gridded precipitation datasets derived from interpolation techniques is highly dependent on the density of local meteorological stations. In regions with sparse observations, such as the western Tibetan Plateau, interpolated products are often subject to substantial uncertainty (Kumar *et al.*, 2021). Due to harsh environmental conditions and limited accessibility, conducting in-situ observations at high altitudes remains challenging, resulting in a scarcity of reliable ground-based data. On the Tibetan Plateau, this shortage of observations leads to systematic underestimation in interpolated precipitation estimates at high elevations (Li, H. *et al.*, 2018; Ménégoz *et al.*, 2013; Yatagai *et al.*, 2012). Moreover, conventional interpolation algorithms, such as Kriging, assume linear precipitation variations and therefore fail to capture the nonlinear orographic effects—such as those caused by canyons and windward slopes—that dominate the plateau's complex terrain (Bhardwaj *et al.*, 2017; Bharti and Singh, 2015; Khandu *et al.*, 2016), These limitations collectively degrade the performance of interpolation-based precipitation products, particularly in the western Tibetan Plateau..

Geographic and environmental factors affect the estimation and retrieval of precipitation in satellite-based precipitation products, leading to variations in detection accuracy across different temporal scales and regional applicability. (Andermann *et al.*, 2011; Bharti and Singh, 2015; Cheng *et al.*, 2025; Duncan and Biggs, 2012; Hamza *et al.*, 2020, 2020; Jena *et al.*, 2020; Kumar *et al.*, 2021; Lyu *et al.*, 2024). These products typically retrieve precipitation from cloud-top brightness temperature, yet the weak and indirect physical relationship between brightness temperature and surface rainfall often introduces substantial retrieval errors (Chen, S. *et al.*, 2013; Gebregiorgis and Hossain, 2015; Maggioni *et al.*, 2017). Although satellite datasets are commonly calibrated against in-situ observations, this calibration is less effective in regions with sparse ground networks. On the Tibetan Plateau, particularly in its western part, the scarcity of observations undermines calibration performance, limiting the reliability of satellite-based estimates (Huffman *et al.*, 2010; Shah and

https://doi.org/10.5194/essd-2026-278
Preprint. Discussion started: 19 June 2026

Mishra, 2016). While satellites offer improved spatial representation of precipitation patterns, they face considerable challenges in accurately capturing precipitation extremes. This is partly due to the limited sensitivity of satellite sensors to low-level clouds and the smoothing effects inherent in retrieval algorithms, which tend to dampen precipitation peaks(Arulraj and Barros, 2019; Bhatt *et al.*, 2014; Oliveira *et al.*, 2016). Additionally, the satellite era began only in the 1980s, which constrains their utility for long-term precipitation studies extending before this period.

Reanalysis datasets are generated by integrating multiple sources of observations with numerical weather prediction models through data assimilation techniques. Through iterative optimization, they produce spatially and temporally continuous precipitation fields that are constrained by physical laws. Compared to interpolated or satellite-based products, reanalysis data offer stronger physical coherence (Baudouin *et al.*, 2020; Wu, X. *et al.*, 2023). However, their performance is limited over the Tibetan Plateau, particularly in the central and western regions, where the scarcity of in-situ observations hampers effective data assimilation. Furthermore, the physical parameterizations within reanalysis models tend to smooth precipitation intensity variations, leading to spatial homogenization of precipitation fields (Di *et al.*, 2015; Tong *et al.*, 2014; Yuan *et al.*, 2021). In these models, precipitation is often strongly parameterized as a function of elevation, yet the schemes are poorly adapted to the plateau's complex atmospheric circulation. This mismatch frequently results in a systematic wet bias at medium to high altitudes.. (Baudouin *et al.*, 2020; Jiang *et al.*, 2021; Silva *et al.*, 2011)。

Currently, no single precipitation dataset performs optimally across the entire Tibetan Plateau (TP), as traditional data production techniques—each with inherent limitations—constrain the reliability of precipitation estimates, particularly in its western region (Lyu *et al.*, 2024). In recent years, the growing application of deep learning (DL) and machine learning (ML) in meteorology has opened new avenues for overcoming these limitations. Architectures such as convolutional neural networks (CNNs) (Shi *et al.*, 2015), Long Short-Term Memory networks (LSTM) (Hochreiter and Schmidhuber, 1997), their spatio-temporal hybrid architecture ConvLSTM (Shi *et al.*, 2015), Transformer (Vaswani *et al.*, 2017) , and the attention mechanism (Attention) (Vaswani et al., 2017) have all been successfully applied to tasks including radar echo extrapolation, satellite retrieval, and site interpolation. For instance, Wu et al. (2020) integrated TRMM satellite data with in-situ observations using a CNN-LSTM hybrid framework, achieving a 26.4% reduction in RMSE over data-sparse regions. More recently, Liu et al. (2024) proposed a Multi-Level Transformer Fusion (MLTF) model that leverages multi-head attention to capture cross-source interactions among TRMM, digital elevation model (DEM), and cloud-top temperature data. In the sparsely observed source region of the Yellow River, their approach improved the correlation coefficient (CC) between estimated and observed precipitation by 19.2% and reduced RMSE by 27.1%. These studies demonstrate that deep learning methods can effectively exploit nonlinear spatiotemporal dependencies in multi-source data,

https://doi.org/10.5194/essd-2026-278
Preprint. Discussion started: 19 June 2026

substantially enhancing the accuracy of precipitation estimates. Numerous studies have developed gridded precipitation fusion frameworks based on machine or deep learning. For instance, Gavahi et al. (2023) proposed the PDFN framework, which integrates 3D-CNN and ConvLSTM to fuse seven datasets—including IMERG and CPC—at 0.1° resolution over the United States, achieving a 35% reduction in MSE and a 16% increase in PCC compared to the best single product. Zhang et al. (2021) employed a dual-machine learning strategy combining Random Forest, Artificial Neural Networks, and Support Vector Machines to correct biases in TRMM and GPM, producing a 1 km daily precipitation dataset across China with a correlation coefficient (CC) of 0.85 against station observations. Ma et al. (2018) applied Dynamic Bayesian Model Averaging (BMA) to fuse multi-satellite precipitation over the Tibetan Plateau (TP), improving the Critical Success Index (CSI) by more than 20%. Despite these advances, most existing frameworks adopt a "site-grid" perspective, where models are trained solely on local station data and fail to explicitly leverage spatial relationships among sites. This limits their generalization capability, particularly in the western TP where in-situ observations are extremely sparse. In contrast, recent research has shifted toward a "graph-structure" perspective. Graph Neural Networks (GNNs) and their variants are increasingly being applied in meteorological studies. Yan et al. (2025) introduced graph convolution into climate statistical downscaling for the first time with their CGNN model, which extracts large-scale circulation features via CNN and then applies GNN to capture interactions between stations and spatial grids on the feature map. Coupled with SBMSE losses, this approach significantly reduces extreme precipitation biases. Vatamány and Mehrkanoon (2025) proposed GD-CAF, a framework that models both spatial and temporal correlations through graph dual-stream convolutional attention, achieving superior precipitation nowcasting performance compared to SmaAt-UNet. Similarly, Yousaf et al. (2025) applied T-GNN to post-process WRF model outputs in Italy, integrating static maps and temporal features to raise forecast accuracy from 24% to 34% in complex terrain. These studies demonstrate that GNNs, particularly Graph Attention Networks (GAT), can explicitly model the four-dimensional coupling among stations, grids, topography, and time. This capability offers a promising new pathway for improving precipitation estimation in observation-sparse regions such as the Tibetan Plateau.

Building upon traditional Graph Neural Networks (GNNs), this study adopts a more advanced architecture—the Graph Attention Network (GAT), originally proposed by Veličković et al. at ICLR 2018. GAT is a neural network layer designed to operate directly on graph-structured data. Its core innovation lies in adapting the self-attention mechanism from the Transformer architecture to the graph domain. Specifically, it assigns learnable attention coefficients to each neighbor of a given node, enabling the model to dynamically weight their contributions during neighborhood aggregation. This allows the network to implement a form of "selective attention," focusing on the most relevant neighbors while down-weighting noisy or less informative ones. In contrast to conventional GNNs, which typically rely on static or pre-defined aggregation

https://doi.org/10.5194/essd-2026-278
Preprint. Discussion started: 19 June 2026

115 weights, GAT introduces a dynamic and adaptive weighting scheme. This attention-based mechanism enhances the model's
116 capacity to generalize, particularly in regions with sparse observational data—such as the western Tibetan Plateau—by
117 strengthening the influence of key neighboring nodes and suppressing irrelevant signals.

118 **2. Data**

119 The proposed 3DM dataset integrates 12 precipitation products, including satellite-based retrievals (TRMM,
120 CMORPH-CDR, GPM), station-based interpolated datasets (APHRO, CN05.1, CHM_PRE), and reanalysis datasets
121 (ERA5, TPRRv1), as summarized in Table 1. Topographic information is derived from the ASTER GDEM v2, a high-
122 resolution digital elevation model jointly developed by Japan's Ministry of Economy, Trade and Industry (METI) and the
123 U.S. National Aeronautics and Space Administration (NASA). This dataset is used to model the relationship between
124 precipitation and terrain.

125 Ground-truth observations are obtained from the "Dataset of Daily Surface Observations from Chinese Surface
126 Stations (V3.0)", provided by the National Meteorological Information Center of the China Meteorological Administration
127 (Ren et al., 2012). From this dataset, 134 long-term in-situ stations located on the Tibetan Plateau are used as reference
128 data. To further evaluate the performance of precipitation products in data-sparse regions, two additional independent
129 validation sets are employed: 9 automatic weather stations in the western TP and 53 rain gauge stations across the mid-
130 western TP (see Table 2). The spatial distribution of all stations is illustrated in Figure 1.

131 **Tab 1 Summary of precipitation datasets used in this study**

Data type	Dataset	Version	Spatiotemporal resolution	Unit	Availability period
Interpolation	*APHRO*	*V1801_R1*	*0.25 ° , 1d*	*mm*	*1998-2015*
		This product was generated from Asian rain gauge data (incorporating a high-density network in the Himalayas) using a terrain-aware interpolation method and strict quality control procedures.			
	CN05.1		*0.25 ° , 1d*	*mm*	*1961-2022*
		The dataset is derived from observations at over 2,400 national stations in China, interpolated using the ANUSPLIN algorithm.			
	CHM_PRE	*V1.0*	*0.25 ° ,1d*	*mm*	*1961-2022*
		Using data from 2,839 Chinese stations, this dataset adopts a "precipitation background + ratio field" framework, integrated with monthly precipitation constraints and topographic adjustments.			

https://doi.org/10.5194/essd-2026-278
Preprint. Discussion started: 19 June 2026

Open Access Earth System Science Data Discussions

Satellite / Microwave / Infrared	*CMORPH-CDR*	*V1.0*	*0.25 ° , 1d*	*mm*	*1998-2022*
		The dataset was generated from multiple microwave and infrared precipitation estimates, corrected using the MORPH deformation technique.			
	TRMM	*3B42V7*	*0.25 ° , 1d*	*mm*	*1998-2019*
		The dataset is derived from TRMM retrievals by applying multi-sensor weighting and monthly-scale corrections based on in-situ observations.			
	GPM		*0.1 ° , 1d*	*mm*	*2001-2023*
		This product derives rainfall estimates through the fusion of data acquired from all passive microwave instruments comprising the GPM constellation.			
	PERSIANN-CDR	*V01r01*	*0.25 ° , 1d*	*mm*	*1983-2022*
		This product utilizes the PERSIANN algorithm to retrieve precipitation from GridSat-B1 infrared satellite observations, subsequently adjusted at the monthly scale using GPCP data.			
	GPCP	*V01r03*	*1.0 ° , 1d*	*mm*	*1997-2022*
		This dataset integrates infrared and microwave observations from dozens of geostationary and polar-orbiting satellites, with bias corrections applied using multiple global station networks.			
Integration/Reanalysis	*CMFD*	*V1.6*	*0.1 ° , 1d*	*mm/hr*	*1979-2018*
		This dataset is derived from TRMM 3B42, GLDAS Noah, and ground-based observations across western China through a framework integrating multi-source weighted fusion, PDF matching, and optimal interpolation (OI) bias correction.			
	CMFD	*V2.0*	*0.1 ° , 1d*	*mm*	*1951-2020*
		This product employs ERA5 as the background field and integrates PDF matching, OI bias correction, and deep learning-based super-resolution downscaling (enhancing resolution from 0.25 ° to 0.1 °), alongside explicit rain-snow separation.			
	ERA5		*0.25 ° , 1d*	*m/hr*	*1961-2022*
		This dataset is generated by the ECMWF Integrated Forecasting System (IFS)			
	TPRRv1		*9km, 1d*	*mm*	*1961-2022*
		The dataset is derived from a 9 km WRF model simulation forced by ERA5 reanalysis fields.			

Tab 2 Imformations of Observations for independent verification

Automatic Observation	**Central-Western TP Observations in rainyseason***

https://doi.org/10.5194/essd-2026-278
Preprint. Discussion started: 19 June 2026

Open Access Earth System Science Data Discussions

Number	Validity period	Station	Validity period	Station	Validity period	Station	Validity period
1	2010-2019	*EW01*	2017-2020	*EW20*	2017-2020	*EW18*	2019-2020
2	2010-2019	*EW02*	2017-2020	*EW21*	2018-2020	*EW19*	2017-2020
3	2014-2019	*EW03*	2017-2020	*EW22*	2017-2020	*SN17*	2016-2020
4	2012-2019	*EW04*	2017-2020	*SN01*	2016-2020	*SN18*	2016-2020
5	2012-2019	*EW05*	2017-2020	*SN02*	2016-2020	*SN19*	2019-2020
6	2012-2019	*EW06*	2017-2020	*SN03*	2016-2020	*SN20*	2019-2020
7	2012-2019	*EW07*	2017-2020	*SN04*	2016-2020	*SN21*	2019-2020
8	2012-2019	*EW08*	2017-2020	*SN05*	2017-2020	*SN22*	2019-2020
9	2013-2019	*EW09*	2017-2020	*SN06*	2016-2020	*SN23*	2019-2020
		EW10	2017-2020	*SN07*	2016-2020	*SN24*	2019-2020
		EW11	2017-2020	*SN08*	2017-2020	*SN25*	2018-2020
		EW12	2017-2020	*SN09*	2017-2020	*SN26*	2018-2020
		EW13	2017-2020	*SN10*	2016-2020	*SN27*	2018-2020
		EW14	2017-2020	*SN11*	2017-2020	*SN28*	2017-2020
		EW15	2017-2020	*SN12*	2016-2020	*SN29*	2018-2020
		EW16	2017-2020	*SN13*	2016-2020	*SN30*	2018-2020
		EW17	2017-2020	*SN14*	2016-2020	*SN31*	2018-2020

134 *EW refers to the East-West cross-sectional observation, SN refers to the north-south cross-sectional observation.

135

https://doi.org/10.5194/essd-2026-278
Preprint. Discussion started: 19 June 2026

Open Access Earth System Science Data Discussions

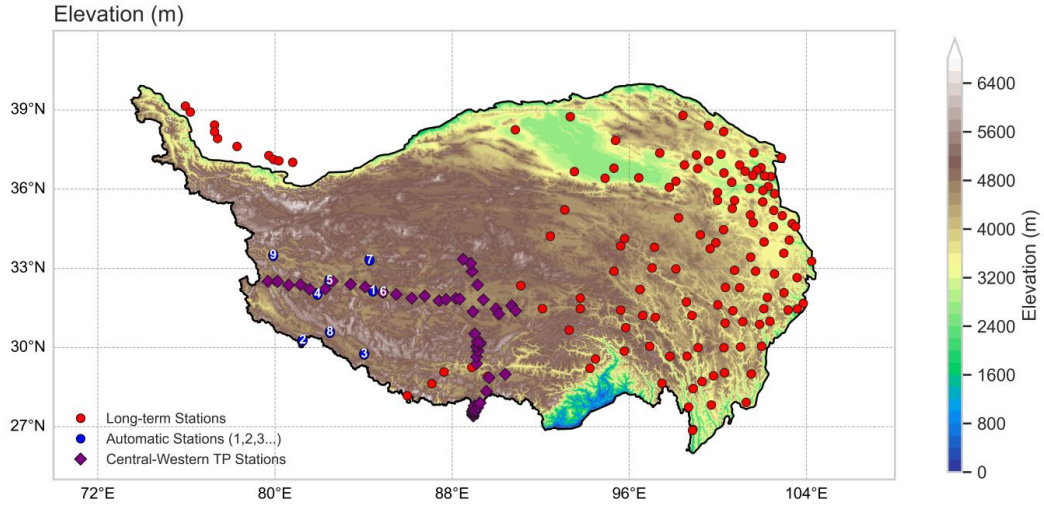

Fig 1 Spatial distribution of observation stations over the Tibetan Plateau, overlaid on an elevation map. The network includes long-term stations (red), automatic stations (blue), and transect rain gauges in the central-western plateau (purple).

2. Methods

3.1 Multi-source Precipitation Fusion Framework

In this study, we propose a deep learning-based framework for fusing multi-source precipitation data, which consists of three main stages—data preprocessing, target location prediction, and post-processing,. The framework is designed to generate a long-term, high-resolution daily precipitation dataset over the Tibetan Plateau. The detailed workflow is as follows.

2.1.1 Data preprocessing

The data preprocessing stage comprises two components: preprocessing of in-situ observations and preprocessing of gridded datasets. Original in-situ precipitation measurements serve a dual purpose: they are used to establish spatial correlations and provide ground-truth labels for the multi-source precipitation fusion model. Precipitation over the Tibetan Plateau is known to follow a Gamma distribution, with a substantial proportion of zero-precipitation events. Training deep learning models directly on precipitation amounts would therefore suffer from a pronounced long-tail effect, impairing model performance. To mitigate this issue, we introduce a climatological perspective by adopting the percentage of

https://doi.org/10.5194/essd-2026-278
Preprint. Discussion started: 19 June 2026

precipitation anomaly as the target variable for model training. To ensure spatial consistency for multi-source data fusion, all 12 precipitation products (Table 1) were resampled to a unified 0.25° × 0.25° grid. This preprocessing step aligns heterogeneous datasets to a common spatial framework, facilitating subsequent integration and comparative analysis. Terrain information from the ASTER GDEM v2 dataset was incorporated, alongside multi-dimensional inputs including station locations, target positions, and daily precipitation anomaly percentages. These elements together form a comprehensive first-level data architecture, enabling robust analysis of precipitation characteristics from diverse perspectives.

Given the requirements of deep learning models for normalized inputs, precipitation data were transformed using logarithmic normalization, reflecting the inherent distribution of precipitation. For terrain data, which exhibits a "peaks + long-tail" distribution, Robust Z-score normalization (median-IQR) was employed. This method effectively mitigates the influence of extreme values, allowing the model to capture meaningful topographic signals without distortion.

2.1.2 Feature Extraction and Target Position Prediction

This stage is composed of two modules: the Graph Attention Network (GAT), responsible for learning spatial relationships among stations, and the Target Position Prediction module, which integrates local features to produce precipitation estimates at target locations.

(1) Graph Attention Network (GAT)

This method constructs a feature map based on the graph-structured relationships among observation sites, incorporating both real site nodes and virtual target nodes. Node features are first optimized using a Transformer, which leverages its powerful self-attention mechanism to capture complex correlations among nodes (sites). This ensures that each node's feature representation incorporates rich global contextual information, thereby producing high-quality initial node features. These enhanced features are then fed into a Graph Attention Network (GAT). After two sequential GAT operations, the node features are updated and propagated. Compared to Graph Convolutional Networks (GCN), GAT assigns different weights to the neighboring nodes of each node via an attention mechanism. The attention weights are calculated as follows:

$$\alpha_{ij} = \frac{\exp\left(\mathrm{LeakyReLU}\left(\vec{a}^{T}\left[W\vec{h}_i \| W\vec{h}_j\right]\right)\right)}{\sum_{k\in\mathcal{N}_i}\exp\left(\mathrm{LeakyReLU}\left(\vec{a}^{T}\left[W\vec{h}_i \| W\vec{h}_k\right]\right)\right)} \quad (1)$$

Where W is the weight matrix to be learned, $\vec{a}$ is the vector to be learned, and LeakyReLU is the activation function. This formula maps the features of node v_i and its neighboring node v_j to a new feature space and calculates their correlation. Through the LeakyReLU activation function, some negative correlation information can be transmitted. Using

https://doi.org/10.5194/essd-2026-278
Preprint. Discussion started: 19 June 2026

Softmax for weight normalization, the sum of the attention coefficients of all neighboring nodes v_i of node v_j is 1, facilitating cross-node comparison of importance. The weighted sum of the eigenvectors h_j of the neighboring nodes v_j of node v_i is calculated based on the normalized attention weights α_{ij}, to obtain the new eigenvector h_i' of node v_i. This eigenvector undergoes a nonlinear transformation through the activation function to obtain the updated node features. The feature update formula is as follows:

$$\overrightarrow{h_i'} = \sigma\left(\sum_{j \in N_i} \alpha_{ij} W \overrightarrow{h_j}\right) \quad (2)$$

This attention mechanism enables the model to automatically learn the importance of relationships between nodes. By aggregating feature information from neighboring nodes, it continuously refines the feature representation of each node, progressively capturing the complex spatial dependencies inherent in precipitation data. The resulting node features are more accurate and comprehensive, enhancing the model's understanding of precipitation distribution within the spatial network structure.

(2) Prediction of Target Position

Based on the extracted global features, the target position prediction is performed. First, the features of the virtual target nodes are isolated and passed through a 3D-CNN fusion layer to achieve local feature extraction and fusion. This process focuses on the target location and its surrounding neighborhood, enabling an in-depth exploration of local precipitation characteristics. By integrating the target node features propagated by the GAT, the model analyzes the similarities, differences, and correlations of precipitation phenomena within the local spatial context, thereby providing more accurate local feature information for the subsequent estimation of precipitation anomaly percentages.

Experimental results confirm that optimal model performance is achieved when extracting spatiotemporal neighborhoods with dimensions of 7 days × 5 grids × 5 grids. Here, "7 days" refers to the time window comprising the target day and the preceding six days, while "5 grids × 5 grids" defines a spatial window centered on the target grid cell, extending two grid cells in each direction. These extracted spatiotemporal blocks are then fed into the 3D-CNN for convolution to estimate precipitation at the target location.

Given the Gamma distribution characteristics of precipitation, we adopt a loss function that extends traditional Mean Squared Error (MSE) by incorporating a Swish-based weighting scheme, referred to as SWMSE. Its calculation formula is as follows:

$$L_{SWMSE} = \frac{1}{N} \sum_{i=1}^{N} Swish(MSE_i) \quad (3)$$

Where $Swish(x) = x \cdot \sigma(x)$, and MSE_i represents the mean squared error for each sample. The advantage is that

https://doi.org/10.5194/essd-2026-278
Preprint. Discussion started: 19 June 2026

the standard MSE is transformed into an adaptive error sensitive loss to cope with data imbalance and tail event neglect problems.

2.1.3 Post-processing

In the post-processing stage, daily optimal data sources are first selected based on in-situ observations. Prior to this, Cumulative Distribution Function (CDF) constraints are applied to the model estimates to ensure robustness across precipitation events of varying intensities. The model estimates are then combined with the selected daily optimal data source through a dynamic weighting scheme, where weights are allocated based on the relative errors of each component. This approach fully accounts for the reliability and accuracy of different data sources, adaptively adjusting their contributions to effectively integrate the strengths of both the original datasets and the model estimates. The final output is a daily precipitation dataset over the Tibetan Plateau with a spatial resolution of 0.25° × 0.25°.

https://doi.org/10.5194/essd-2026-278
Preprint. Discussion started: 19 June 2026

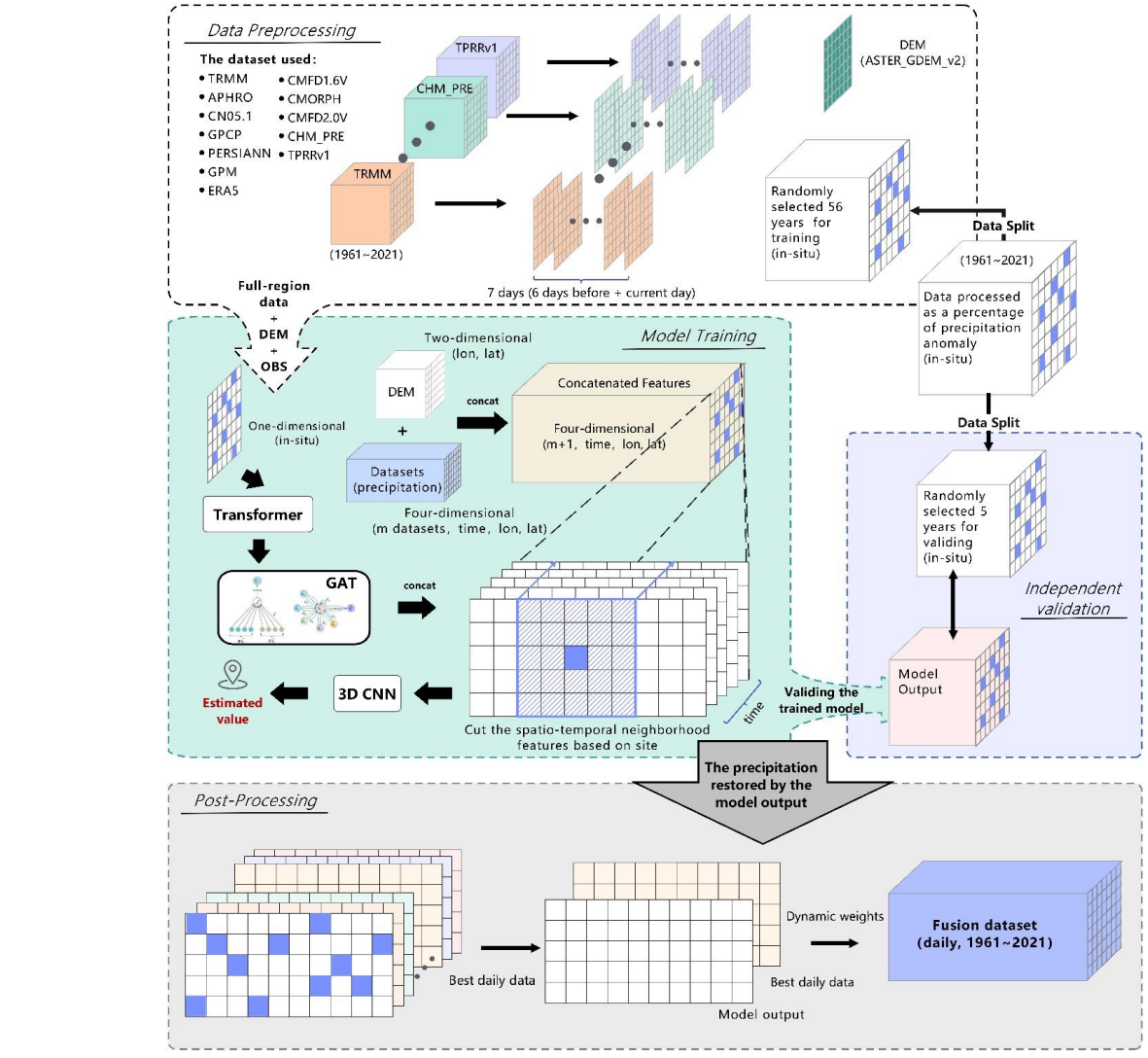

Fig 2 Multi-source Precipitation Fusion Framework

2.2 Evaluation Metrics

A set of evaluation metrics (Table 3) are employed to assess the multi-source precipitation datasets from multiple perspectives, including precipitation amount, event identification capability, and overall accuracy. These metrics —

https://doi.org/10.5194/essd-2026-278
Preprint. Discussion started: 19 June 2026

227 covering correlation, systematic bias, hit rate, missed reports, and false alarms—form a multi-dimensional evaluation
228 system. It not only reveals the strengths and limitations of different precipitation products across various aspects, but also
229 provides a scientific basis for product improvement, fusion algorithm optimization, and dataset selection for specific
230 application scenarios such as flood forecasting, agricultural irrigation, and climate research.

231 **Tab 3 List of statistical and classification metrics for evaluating**

Metrics	Instruction	Formula	Unit	Interval	Best Value
CC	The linear correlation between observations and estimates	$CC = \frac{\sum_{i=1}^{N}(\lvert P_i - \bar{P}\rvert)(\lvert O_i - \bar{O}\rvert)}{\sqrt{\sum_{i=1}^{N}(\lvert P_i - \bar{P}\rvert)^2} \times \sqrt{\sum_{i=1}^{N}(\lvert O_i - \bar{O}\rvert)^2}}$	mm	[-1~1]	1
BIAS	The ratio of estimated and observed frequencies	$BIAS = \frac{H+F}{H+M}$	/	[0~∞)	1
ME	The mean systematic deviation of estimates relative to observations	$ME = \frac{1}{N}\sum_{i=1}^{N}(P_i - O_i)$	mm	(-∞,+ ∞)	0
FAR	Proportion of events that are detected but not observed	$FAR = \frac{F}{H+F}$	/	[0~1]	0
POD	Proportion of events observed and detected	$POD = \frac{H}{H+M}$	/	[0~1]	1
POFD	Proportion of events detected but not observed	$POFD = \frac{F}{F+C}$	/	[0~1]	0
CSI	Proportion of correctly estimated events	$CSI = \frac{1}{\left(\frac{1}{1-FAR}\right)+\left(\frac{1}{POD}\right)-1}$	/	[0~1]	1
MSE	The degree of discrepancy between estimation and observation	$MSE = \frac{1}{m}\sum_{i=1}^{m}(P_i - O_i)^2$	mm^2	[0~∞)	0

232 P_i: Precipitation estimate; O_i: Precipitation observation; $\bar{P}$: Mean of precipitation estimates; $\bar{O}$: Mean of precipitation observation; N:
233 Number of valid samples; H: Hits (precipitation observed and correctly detected); F: False (no precipitation observed but precipitation
234 detected); M: Miss (precipitation observed but not detected); C: Correct negatives (no precipitation observed and none detected).
235

236 **3. Dataset Evaluation**

https://doi.org/10.5194/essd-2026-278
Preprint. Discussion started: 19 June 2026

Evaluation of the 3DMergePrec (3DM) dataset encompasses multiple dimensions, including total precipitation, precipitation frequency, and extreme precipitation characteristics. To enable consistent intercomparison, the study period was constrained to years common to all products: 2001 – 2015 for long-term observations, 2010 – 2015 for western automatic observations, and 2016 – 2020 for the central-western transect rain gauges. Notably, the western automatic stations and transect rain gauges were not incorporated into the fusion procedure and thus serve as fully independent validation datasets.

4.1 Validation Results Against Long-Term In-Situ Observations

The probability distribution of precipitation (Fig. 3) reveals that the probability of precipitation over the Tibetan Plateau decreases with increasing precipitation intensity. The probability is highest for intensities below 0.5 mm and declines rapidly thereafter. The probability distribution of 3DM exhibits a distinct inflection point at 14 mm. For intensities below 14 mm, 3DM shows higher probabilities than observed, with a slight overestimation in the 1–8 mm range (approximately 10^{-2} to 10^{-1}), indicating a mild overestimation of light precipitation frequency. In the 8 – 14 mm interval, the 3DM curve closely aligns with observations, suggesting that the fusion framework successfully preserves the cumulative probability morphology within this range.

In contrast, other datasets generally overestimate the probability of intensities below 14 mm and exhibit substantial variability for intensities exceeding 14 mm. For precipitation intensities greater than 20 mm, 3DM shows a downward deviation relative to observations, with its probability estimates only closer to observations than those of APHRO and CN05.1. This indicates that 3DM tends to slightly underestimate overall precipitation and systematically underestimates extreme events. This underestimation can be attributed to the scarcity of extreme precipitation samples in the training dataset, combined with the smoothing effect of the Gamma transformation on the tail of the distribution.

Based on the above analysis, 3DM tends to overestimate the probability of light rain, while underestimating the probabilities of moderate and heavy rain, with a notable underestimation of extreme precipitation events. Nevertheless, the overall shape of the 3DM cumulative distribution function closely follows that of the observations, indicating that the product retains robustness in representing the general statistical characteristics of precipitation over the Tibetan Plateau.

https://doi.org/10.5194/essd-2026-278
Preprint. Discussion started: 19 June 2026

Open Access Earth System Science Data Discussions

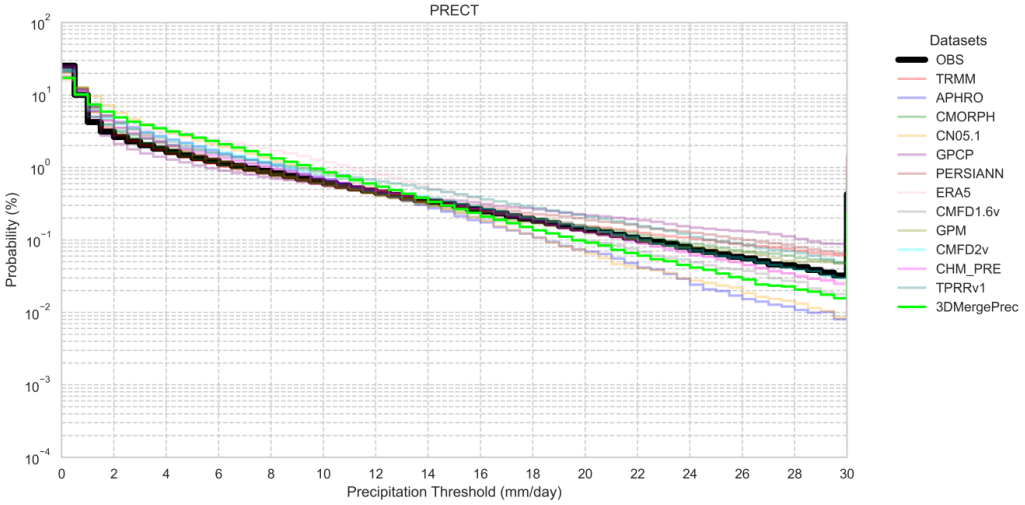

Fig 3 The Probability Distribution of the precipitation datasets (2001-2015)

The Critical Success Index (CSI) is a statistical metric used to evaluate the performance of binary classification models, such as the detection of precipitation events (presence or absence) based on a specified threshold. CSI values range from 0 to 1, where 1 represents a perfect prediction and 0 indicates no skill beyond random chance. In this study, a threshold of 0.1 mm is applied to define a precipitation event. The CSI was calculated for each dataset to assess its ability to correctly identify the occurrence or non-occurrence of precipitation over the Tibetan Plateau. As shown in Fig. 4, similar to most datasets, the CSI of 3DM generally ranges from 0.30 to 0.80 across the main body of the Tibetan Plateau, demonstrating good spatial continuity—a favorable characteristic for regional climate model validation. Although CSI values decrease to 0.25 – 0.40 in the northwestern margin of the plateau, they remain notably higher than those of several non-interpolated datasets (e.g., TRMM, CMFD2v, GPCP, CMORPH), indicating that 3DM retains a relatively better capability for capturing precipitation events in this region.In the southwestern and northwestern TP, most datasets exhibit CSI values generally below 0.4. This may be attributed to the complex terrain and sparse observational networks in these areas. Complex topography can lead to heterogeneous precipitation distributions, while limited station coverage may reduce the representativeness of the data, thereby affecting CSI calculations.

Notably, the high-CSI regions across all datasets largely coincide with areas of high mean squared error (MSE) (Fig. 5), suggesting that the primary source of error lies in the quantitative estimation of precipitation magnitude rather than in event identification. This implies that while the model performs well in identifying precipitation occurrence, uncertainties

https://doi.org/10.5194/essd-2026-278
Preprint. Discussion started: 19 June 2026

persist in accurately estimating precipitation amounts.

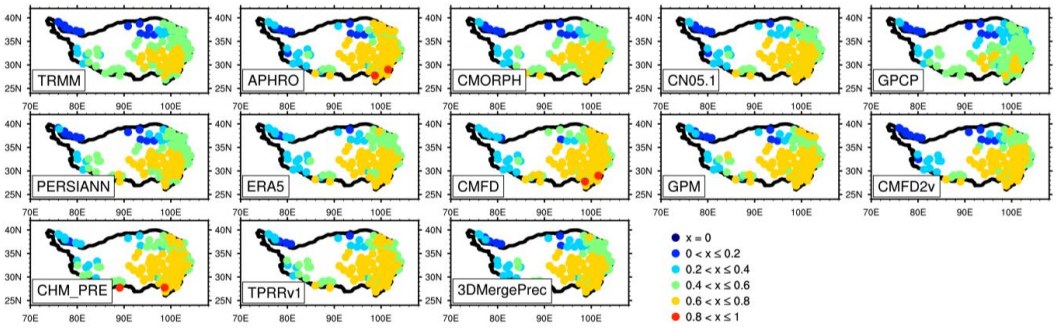

Fig 4 Spatial distributions of the Critical Success Index (CSI) representing rain/no-rain detection performance across multiple datasets, 2001 – 2015

Evaluation based on long-term observations reveals pronounced spatial heterogeneity in the mean squared error (MSE) of precipitation estimates across most datasets during the 2001 – 2015 rainy season (Fig. 5). Satellite-based and satellite-reanalysis fusion products—including TRMM, GPCP, CMORPH, PERSIANN, and GPM—exhibit a prominent error belt exceeding 30 mm^2 in the southeastern Tibetan Plateau. This belt extends from the northeastern plateau (near Qinghai Lake) to the southwestern plateau (near the Yarlung Zangbo Grand Canyon), with errors progressively increasing toward the southeast. These areas are characterized by relatively lower elevations and higher precipitation amounts compared to the plateau average, posing challenges for satellite-based precipitation estimation. In contrast, 3DM maintains MSE values generally below 20 mm^2 across the main body of the plateau. Concentrated errors exceeding 25 mm^2 only appear in regions with steep terrain gradients exceeding 1000 m per 50 km, such as the northern slope of the Nyenchen Tanglha Mountains and the Hengduan Mountains. Based on 134 long-term in-situ stations, the mean rainy-season MSE of 3DM is 28.53 mm^2, representing a 30 – 40% reduction compared to satellite products such as TRMM (41.37 mm^2), GPM (38.92 mm^2), and CMORPH (45.21 mm^2). Furthermore, the number of stations exhibiting high errors is reduced by approximately half.

Overall, 3DM demonstrates clear advantages over most non-interpolated precipitation datasets (including satellite products, GPCP, PERSIANN, and CMFD2v) in terms of rainy-season MSE based on long-term observations. Its errors are substantially smaller, and stations with large errors are relatively few, primarily concentrated along the southeastern margin of the Tibetan Plateau.

https://doi.org/10.5194/essd-2026-278
Preprint. Discussion started: 19 June 2026

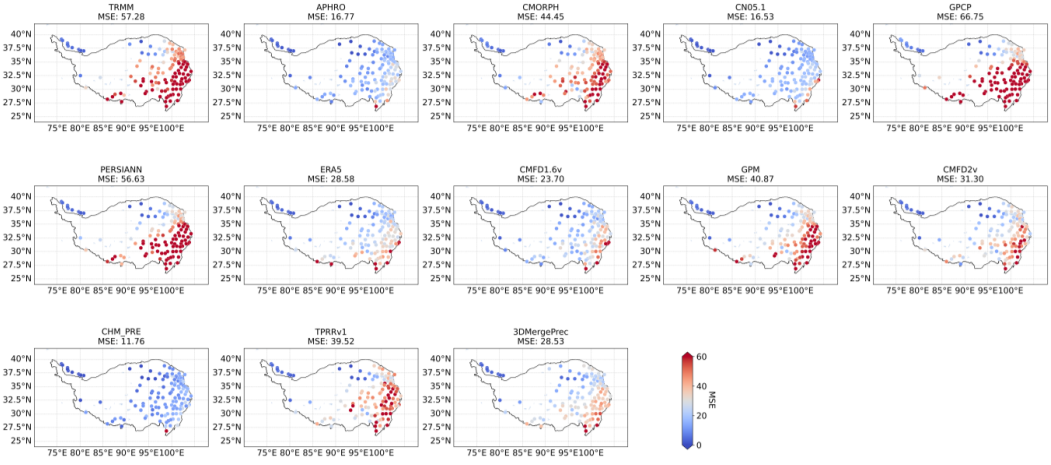

Fig 5 The spatial distribution of the MSE of precipitation estimations during the rainy season in 2001~2015

As shown in Fig. 6, the scatter cloud of 3DM based on long-term observations exhibits an ellipsoidal distribution aligned along the 1:1 diagonal line, with an RMSE of 5.34 mm/d and a ME of 0.78 mm/d. Compared to the fan-shaped scatter distributions of satellite products such as TRMM and GPM (RMSE: 6.5–7.8 mm/d; ME: 0.5–1.1 mm/d), the 3DM scatter cloud is more tightly clustered around the 1:1 line, with notable reductions in both RMSE and bias. This indicates that the proposed fusion framework effectively reduces systematic errors and enhances consistency between estimated and observed precipitation.

However, 3DM still exhibits higher errors than interpolation-based datasets such as CHM_PRE, CN05.1, and APHRO (Fig. 6), suggesting room for further improvement in precipitation accuracy. The major axis of the 3DM ellipsoidal scatter cloud shows a slight tilt toward the observation axis, with most points concentrated in the 0 – 20 mm range, indicating reliable performance for light to moderate precipitation events. In contrast, scatter points corresponding to precipitation greater than 20 mm are systematically shifted downward, reflecting a compression of extreme precipitation estimates. This underestimation is directly attributable to the scarcity of extreme precipitation samples in the training dataset and the smoothing effect of the Gamma transformation on the tail of the distribution.

The relatively wide spatial coverage of the 3DM scatter cloud also suggests uncertainty in the model's ability to precisely localize heavy precipitation events. Future improvements could benefit from incorporating physical constraints specifically targeting heavy precipitation, or employing loss functions that assign greater weight to extreme events, thereby narrowing the error range and improving extreme precipitation representation.

https://doi.org/10.5194/essd-2026-278
Preprint. Discussion started: 19 June 2026

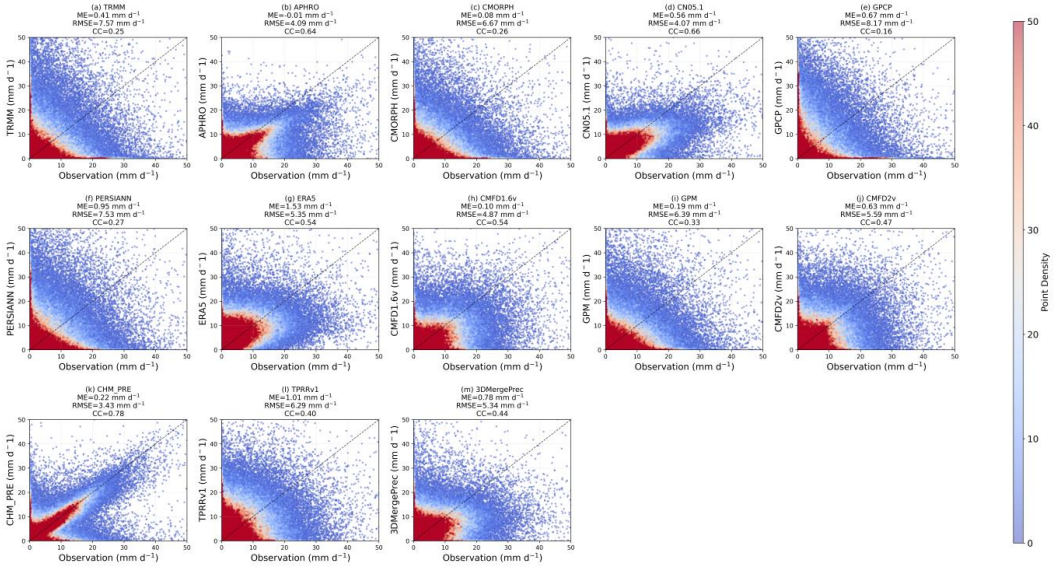

Fig 6 Density-based scatter plot comparing estimated and observed daily precipitation during the rainy season for the stations with long-term observations (2001 – 2015). The diagonal black line marks the 1:1 reference, and the color gradient represents the relative density of data points.

Given that gridded precipitation datasets commonly overestimate light precipitation, this study further calculates the mean precipitation frequency for intensities below 10 mm based on long-term observations (Fig. 7), aiming to evaluate the performance of each dataset in characterizing light precipitation events. The results indicate that 3DM reasonably reproduces the mean precipitation frequency characteristics across different intensity classes. In the weak precipitation range (0 – 5 mm/d), the frequency estimated by 3DM is higher than the observed values, suggesting a potential overestimation of precipitation occurrence, particularly in the 0.75 – 5.0 mm/d interval. In contrast, other datasets—such as TRMM, CMORPH, and GPCP—tend to underestimate precipitation frequency relative to observations, implying a risk of underestimation or missed events. Overall, satellite-based datasets perform best in estimating precipitation frequency below 10 mm. Although 3DM exhibits a slight overestimation, its frequency distribution pattern remains broadly consistent with the observed pattern, indicating that 3DM can effectively capture the probability characteristics of light precipitation across different intensity levels.

https://doi.org/10.5194/essd-2026-278
Preprint. Discussion started: 19 June 2026

Open Access Earth System Science Data Discussions

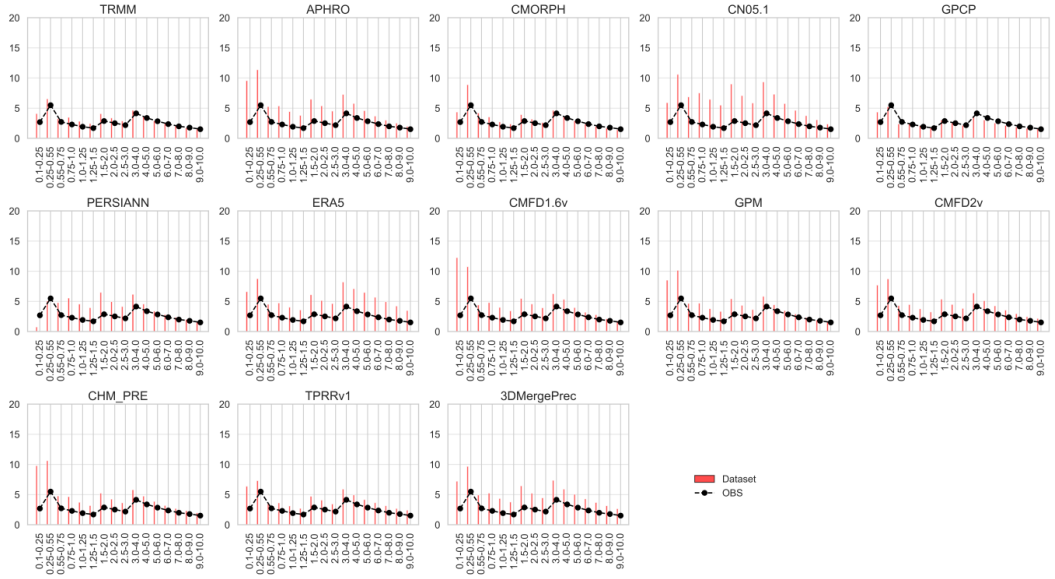

Fig 7 Distribution of mean precipitation frequency for various intensities that are below 10 mm based on long-term in-situ observations (2001 – 2015). Red bars represent the frequencies estimated by each precipitation product, and black lines indicate the observed frequencies.

Figure 8 presents the boxplot distributions of BIAS, FAR, POD, POFD, and CSI during the rainy season for the long-term observation period 2001–2015. These metrics evaluate the capability of each dataset to capture precipitation events, with a threshold of 0.1 mm defining a precipitation day. Based on long-term observations, the 3DM fusion dataset achieves a median Probability of Detection (POD) of 0.95, False Alarm Ratio (FAR) of 0.40, and Critical Success Index (CSI) of 0.60, performing generally better than most satellite-based datasets. This indicates that 3DM can effectively detect actual precipitation events with a relatively high proportion of correct detections, reflecting favorable accuracy and reliability. The high POD value suggests that the fusion framework exhibits strong sensitivity to precipitation occurrence, which can be attributed to the Graph Neural Network architecture adopted in this study. By explicitly modeling the spatial relationships between stations, the GAT enhances the model's ability to capture precipitation signals. However, the median FAR of 3DM is 0.4, slightly higher than that of other datasets. This indicates that 3DM occasionally misclassifies non-precipitation periods as precipitation events. Such false alarms may be related to the amplification of light precipitation probabilities induced by the Gamma transformation, meaning that the model tends to erroneously identify non-precipitation conditions as precipitation events under weak precipitation regimes.

https://doi.org/10.5194/essd-2026-278
Preprint. Discussion started: 19 June 2026

Open Access Earth System Science Data Discussions

356 Overall, the precipitation event detection capability of 3DM, as evaluated against long-term observations, is inferior
357 to interpolation-based datasets but markedly superior to satellite datasets. It ranks near the median among all datasets and
358 demonstrates stable and consistent performance.

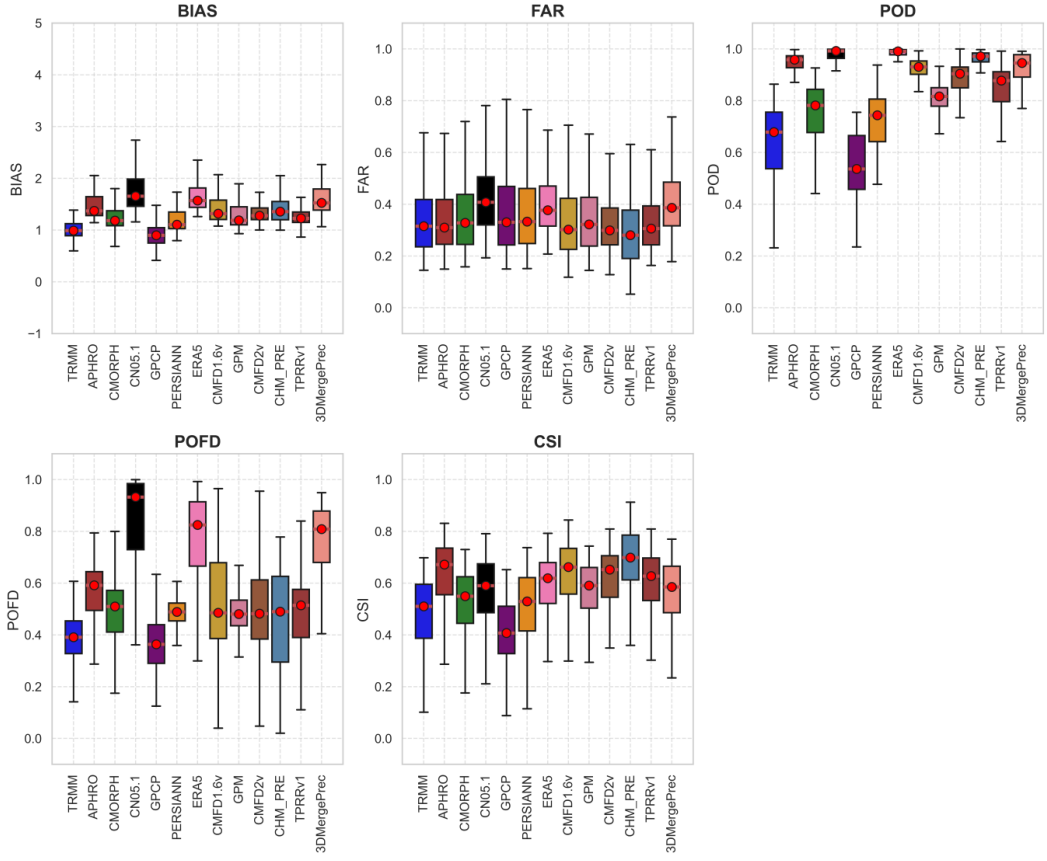

359
360 **Fig 8 Statistical summary of precipitation event detection metrics evaluated against long-term observations (2001 – 2015). Each**
361 **boxplot displays the interquartile range (25th – 75th percentiles), capturing the central 50% of station-level metric values. The**
362 **red dot represents the median, and the whiskers extend to the minimum and maximum values, indicating the full spread of the**
363 **data.**
364
365 To further investigate the performance of each dataset in capturing both the intensity and long-term trends of regional-
366 mean precipitation, the Tibetan Plateau was divided into eastern and western parts along 90° E (Fig. 9). The results indicate
367 that most datasets tend to overestimate precipitation over the plateau. In the eastern TP, precipitation generally exhibits an

https://doi.org/10.5194/essd-2026-278
Preprint. Discussion started: 19 June 2026

368 increasing trend, with an observed rate of 0.07 mm/d per decade. The fusion product 3DM shows a trend of 0.05 mm/d per
369 decade, which passes the significance test. Although slightly lower than the observed value, the 3DM trend closely aligns
370 with observations. Among long-term datasets, its performance is comparable to CMFD2v and clearly superior to most
371 other products, demonstrating that 3DM can effectively capture precipitation variations over the eastern TP.

372 As shown in Fig. 10, the observed precipitation trend over the western TP is 0.05 mm/d per decade. The trend derived
373 from 3DM is consistent with observations in sign and passes a more stringent significance test. Compared with other long-
374 term datasets—many of which either underestimate or misrepresent the precipitation trend over the western TP—3DM
375 achieves the trend closest to observations, enabling a more reliable representation of regional precipitation trends in this
376 data-sparse region. These findings suggest that the proposed fusion framework effectively improves the representation of
377 precipitation trends over the western Tibetan Plateau.

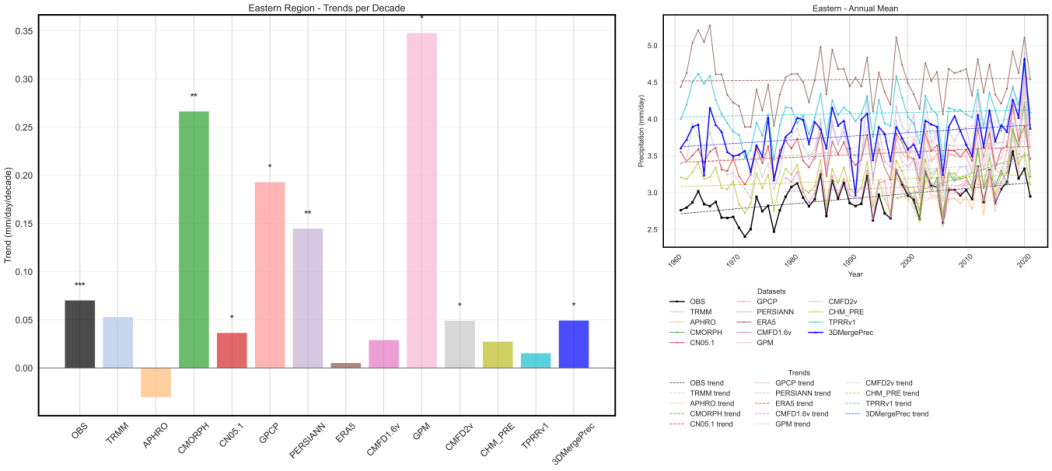

378

379 **Fig 9 Linear trend and time series of the regional-mean precipitation over the eastern Tibetan Plateau for different datasets and**
380 **long-term in-situ observations. The left panel shows the trend of each dataset per decade (unit: mm/day/decade), and "***",**
381 **"**", "*" respectively mean that the level of significance tests at 0.001, 0.01, and 0.05, dataset has passed. The right panel Ime**
382 **series of annual mean precipitation (mm/d) from each dataset, with dotted lines illustrating the corresponding linear trends.**

https://doi.org/10.5194/essd-2026-278
Preprint. Discussion started: 19 June 2026

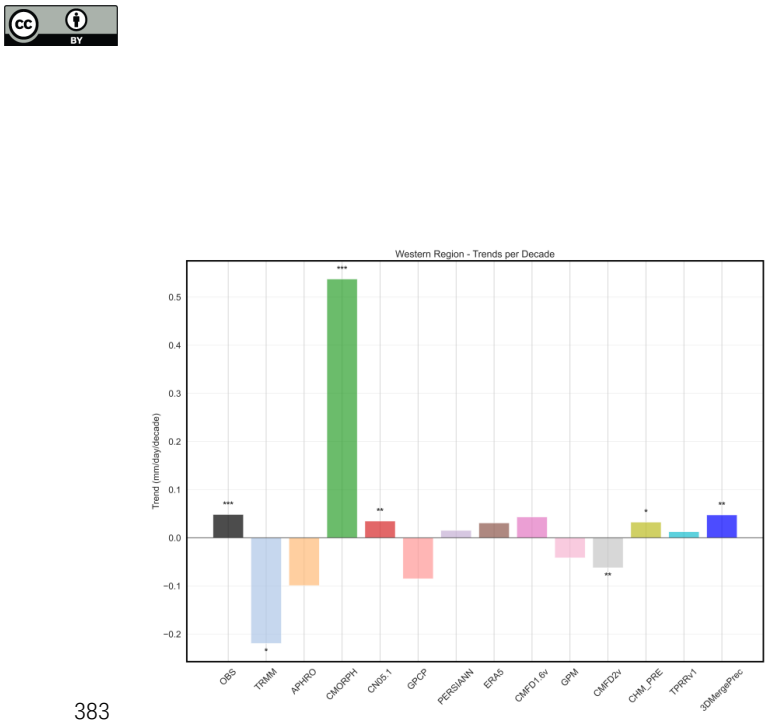

Fig 10 Same as Figure 9, but for western TP.

4.2 Independent Evaluation Based on Western Tibetan Plateau Ground Observations

The evaluation based on long-term observations indicates that the 3DM dataset exhibits error characteristics over the western uninhabited regions (e.g., Changtang and Ngari Prefecture) similar to those observed over the central TP (Fig. 5). To further assess its performance in data-sparse areas, 9 automatic weather stations and 53 rain gauges across the western TP were employed for independent validation. Based on the 9 automatic stations, the average MSE of 3DM is 10.78 mm^2 (Table 4), representing a 26% – 52% reduction in error compared to datasets such as TRMM, GPCP, and PERSIANN. It ranks fourth among all evaluated datasets and performs substantially better than CHM_PRE, CMFD2v, and most other products, confirming that the proposed fusion framework remains credible and reliable even in observation-sparse regions. Validation using the 53 rain gauges (Table 4) further demonstrates that 3DM outperforms most datasets in reproducing the spatial gradient of precipitation between the central and western TP, achieving an overall MSE of 17.09 mm^2 and ranking second overall. However, 3DM exhibits relatively larger errors over the central – southern plateau, with an MSE of 69.39 mm^2, ranking seventh among datasets. Examination of individual station records reveals that these errors predominantly originate from the central TP—a pattern consistent with most existing datasets—suggesting that such biases may be inherited from the input source products.

Moreover, the central TP functions as a climatic transition zone with limited in-situ observations. The current fusion framework, driven solely by multi-source precipitation datasets and terrain information, lacks dynamic physical constraints

https://doi.org/10.5194/essd-2026-278
Preprint. Discussion started: 19 June 2026

to adequately represent the region's complex precipitation characteristics. Future work will aim to incorporate dynamical mechanisms to improve precipitation estimation in this area.

Overall, the 3DM dataset demonstrates clear improvements in precipitation estimation over the western TP and effectively captures the central–western precipitation gradient. Despite remaining biases in the central TP, the proposed fusion framework achieves substantial overall optimization for precipitation estimation across the western Tibetan Plateau.

Tab 4 MSE during the rainy season over the western TP (2010–2015)

Datasets/Station Number	Observations at automatic stations（2010-2015）										Rainy-Season Observations over the Central-Western TP (2016–2020)	
	1	2	3	4	5	6	7	8	9	Mean	EW Mean	SN Mean
3DMergePrec	17.64	7.19	8.34	8.47	8.59	8.67	6.41	11.88	19.83	10.78	17.09	69.39
APHRO	17.86	8.10	7.76	7.75	7.78	13.77	4.25	4.10	5.01	**8.49**	-	-
CHM_PRE	16.63	10.44	12.40	22.76	16.89	34.35	8.46	22.28	8.92	17.01	20.27	23.90
CMFD1.6v	11.92	**5.13**	7.75	24.69	10.01	6.26	9.40	6.82	**3.99**	9.55	24.73	29.35
CMFD2v	18.43	7.82	6.67	9.73	6.87	18.58	6.56	**2.50**	20.56	10.86	24.98	46.37
CMORPH	17.13	6.09	8.65	45.30	8.02	**4.34**	4.77	13.79	10.02	13.12	122.56	109.80
CN05.1	14.48	7.22	8.27	11.23	9.56	7.26	3.66	13.58	6.93	9.13	**13.38**	**22.96**
ERA5	17.11	7.96	8.42	9.44	9.38	13.30	4.39	14.31	31.63	12.88	19.97	162.85
GPCP	41.15	41.68	19.45	24.81	21.92	40.51	16.78	28.27	39.30	30.43	42.27	82.99
GPM	**10.13**	7.15	**5.33**	**6.93**	**5.81**	10.60	3.83	10.59	58.63	13.22	26.47	45.31
PERSIANN	34.43	17.19	14.69	17.85	12.21	25.88	11.86	22.20	39.53	21.76	105.59	99.64
TPRRv1	21.51	9.20	7.29	12.83	10.18	13.64	**3.38**	12.47	23.98	12.72	28.14	48.73
TRMM	17.44	7.36	8.16	58.40	9.62	21.72	7.50	18.49	27.36	19.56	23.16	108.55

- means no data, EW refers to the East-West cross-sectional observation, SN refers to the north-south cross-sectional observation.

As shown in the scatter density plot of precipitation over the western Tibetan Plateau (Fig. 11), all datasets exhibit a systematic overestimation of precipitation (ME > 0), with values ranging from 0.13 to 1.30 mm/d. This positive bias is also inherited by the fusion dataset. The 3DM product achieves a ME of 0.53 mm/d and an RMSE of 3.36 mm/d, representing a moderate yet competitive overall performance. Among the 12 datasets presented in Fig. 11, the ME of 3DM is notably

https://doi.org/10.5194/essd-2026-278
Preprint. Discussion started: 19 June 2026

lower than that of five satellite and reanalysis products, including TRMM (0.84 mm/d), GPCP (1.04 mm/d), PERSIANN (1.30 mm/d), ERA5 (1.13 mm/d), and CMFD2v (0.75 mm/d). Compared to other non-interpolation-based datasets, 3DM shows only a marginal increase in ME, ranging from 0.01 to 0.02 mm/d. These results suggest that although 3DM incorporates systematic errors from multiple source datasets over the western region, it effectively mitigates severe overestimation. In terms of RMSE, 3DM (3.36 mm/d) is slightly outperformed by APHRO (2.76 mm/d), CMFD1.6v (3.02 mm/d), CMFD2v (3.25 mm/d), and CN05.1 (3.05 mm/d). However, it surpasses all satellite-based datasets, including TRMM (4.56 mm/d), GPM (4.07 mm/d), and CMORPH (3.65 mm/d). This indicates that the proposed fusion framework is capable of reducing random errors in precipitation estimates over the western TP to a certain extent. As revealed by the scatter density pattern, the number of outliers for 3DM increases markedly at precipitation intensities above 4 mm/d, contributing to its higher RMSE compared to APHRO and CN05.1. The correlation coefficient (CC) for 3DM is 0.41, lower than that of CMFD1.6v (0.54) and CMFD2v (0.53). This indicates the presence of spatial positioning errors or magnitude biases for larger precipitation events (exceeding 10 mm/d) over the western TP. These errors are primarily introduced by the fusion framework, which relies on multi-source precipitation datasets and terrain-driven mechanisms. To address this limitation, future work should incorporate dynamic process constraints to mitigate the impact of such systematic errors and further improve precipitation estimation accuracy in the region.

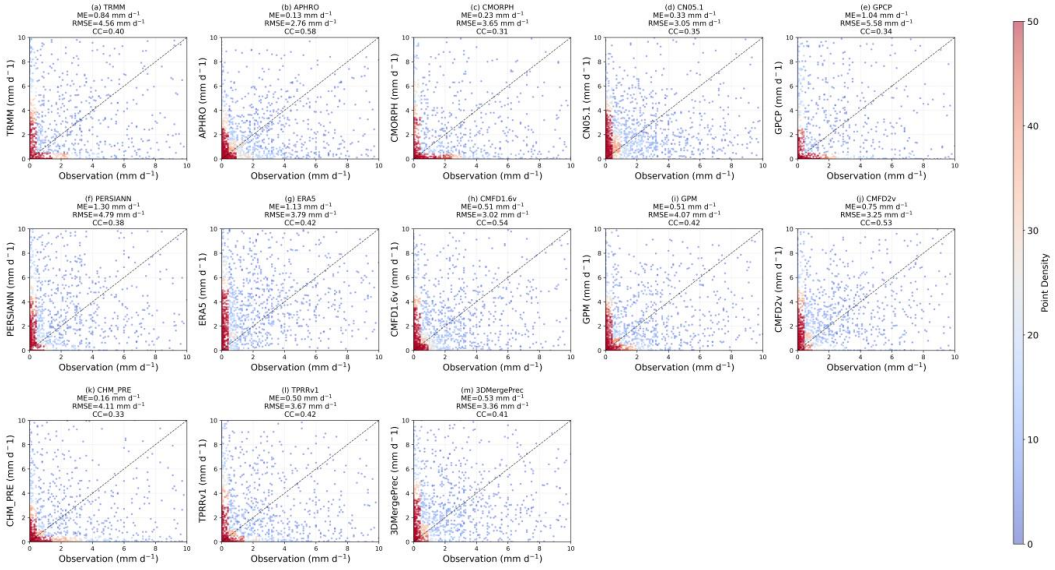

Fig 11 Density-based scatter plot comparing estimated and observed daily precipitation during the rainy season for western TP. The diagonal black line marks the 1:1 reference, and the color gradient represents the relative density of data points.

https://doi.org/10.5194/essd-2026-278
Preprint. Discussion started: 19 June 2026

The frequency of precipitation events across different intensity levels were further analyzed over the western Tibetan Plateau. The results indicate that all datasets tend to overestimate light precipitation frequency relative to observations, reflecting a common bias among existing products. The overestimation of micro-precipitation by 3DM is comparable to that of CMFD2v. Datasets such as APHRO, CN05.1, CMFD1.6v, and ERA5 exhibit pronounced overestimation, particularly for precipitation intensities below 4 mm. In contrast, TRMM and GPCP show the closest agreement with observed precipitation frequencies, suggesting that satellite-based datasets maintain relatively high accuracy and stability in capturing micro-precipitation events over the TP. Nevertheless, these datasets still display notable random errors for precipitation events exceeding 10 mm in the western region (Table 4, Fig. 5). Currently, 3DM continues to overestimate micro-precipitation frequency in the western TP, which may lead to underestimation of dry events. Users should exercise caution when applying this dataset for applications sensitive to light precipitation or dry condition detection.

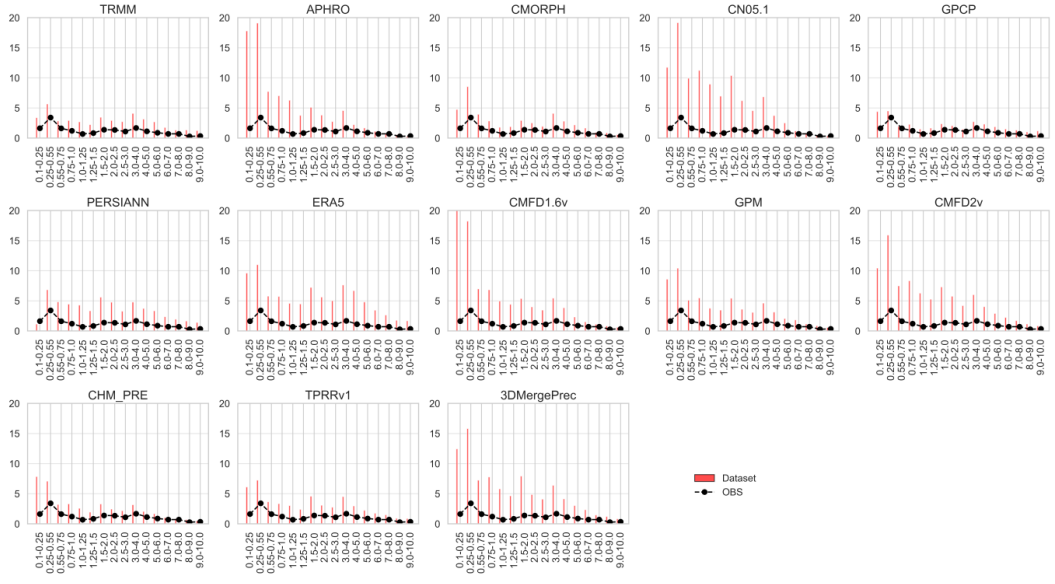

Fig 12 Distribution of mean precipitation frequency for various intensities that are below 10 mm based on observations over western TP. Red bars represent the frequencies estimated by each precipitation product, and black lines indicate the observed frequencies.

The evaluation metrics used in Fig. 13 are identical to those in Fig. 8, but here the samples are derived from independent validation observations in the western TP, focusing exclusively on the capability to capture precipitation events

https://doi.org/10.5194/essd-2026-278
Preprint. Discussion started: 19 June 2026


Open Access Earth System Science Data Discussions

(threshold: > 0.1 mm). Compared to the metrics based on long-term observations (Fig. 8), CSI values in the western region are generally lower. TPRRv1 exhibits the highest CSI in the west (0.58), while 3DM achieves a median CSI of 0.45, comparable to CHM_PRE. Among all datasets, 3DM ranks highly, outperforming most interpolation-based products as well as CMFD1.6v and CMFD2v. However, the wider box plot for 3DM indicates greater uncertainty in its performance. Across all datasets, POD values in the western region decrease by 0.1 – 0.3 relative to the east. The median POD for 3DM drops from 0.96 to 0.82. This decline may be attributed to the fact that most training labels are derived from stations in the eastern plateau, with very few observations available in the west. Although the GAT architecture is employed to capture spatial features, its generalization ability in the western region remains constrained by the limited input data (primarily precipitation and terrain).

All datasets exhibit BIAS values exceeding 1.0, indicating systematic overestimation, and POFD values above 0.15. The spatial pattern of POFD closely mirrors that of BIAS, with both metrics considerably higher than in the eastern region (where POFD < 0.05). The median range of POFD across datasets widens from [0.2 – 0.4] in the east to [0.4 – 0.7] in the west, reflecting a general tendency to overestimate precipitation in this arid region. This overcompensation for sample sparsity leads to increased false alarms. Even TPRRv1, despite achieving the highest CSI, exhibits a median POFD exceeding 0.2, indicating that overestimation remains a challenge.

Notably, 3DM demonstrates optimized POFD performance in the western region, with a higher ranking and reduced median value. Its box plot shows a more concentrated sample distribution, enabling 3DM to maintain a relatively low POFD while ensuring a high POD—a key factor contributing to its improved CSI ranking. This may be related to 3DM's accuracy in precipitation magnitude estimation. Given that precipitation in the western region is generally lighter than in the east, the fusion framework appears to exhibit enhanced sensitivity to micro-precipitation events in this area, a characteristic that is reflected in its estimates.

Based on the comprehensive evaluation metrics, 3DM demonstrates favorable overall performance. Its high POD and CSI values reflect strong sensitivity to precipitation occurrence and reliable accuracy in capturing precipitation events over the western TP. Although the FAR value remains relatively high—indicating some false alarms for light precipitation—the overall performance of 3DM in the western region still surpasses that of most datasets, including CN05.1 and CMFD2v. CN05.1 also achieves a high POD, but its substantially higher POFD tends to induce more false alarms. In contrast, datasets such as CMFD1.6v and CMFD2v exhibit inferior performance to 3DM in the western region.

These evaluation results consistently demonstrate that the proposed fusion framework has played an optimizing role in precipitation estimation over the western Tibetan Plateau. Improvements are evident in precipitation magnitude

https://doi.org/10.5194/essd-2026-278
Preprint. Discussion started: 19 June 2026

Open Access Earth System Science Data Discussions

estimation, trend representation, and event detection capability, confirming the robustness and reliability of the 3DM dataset.

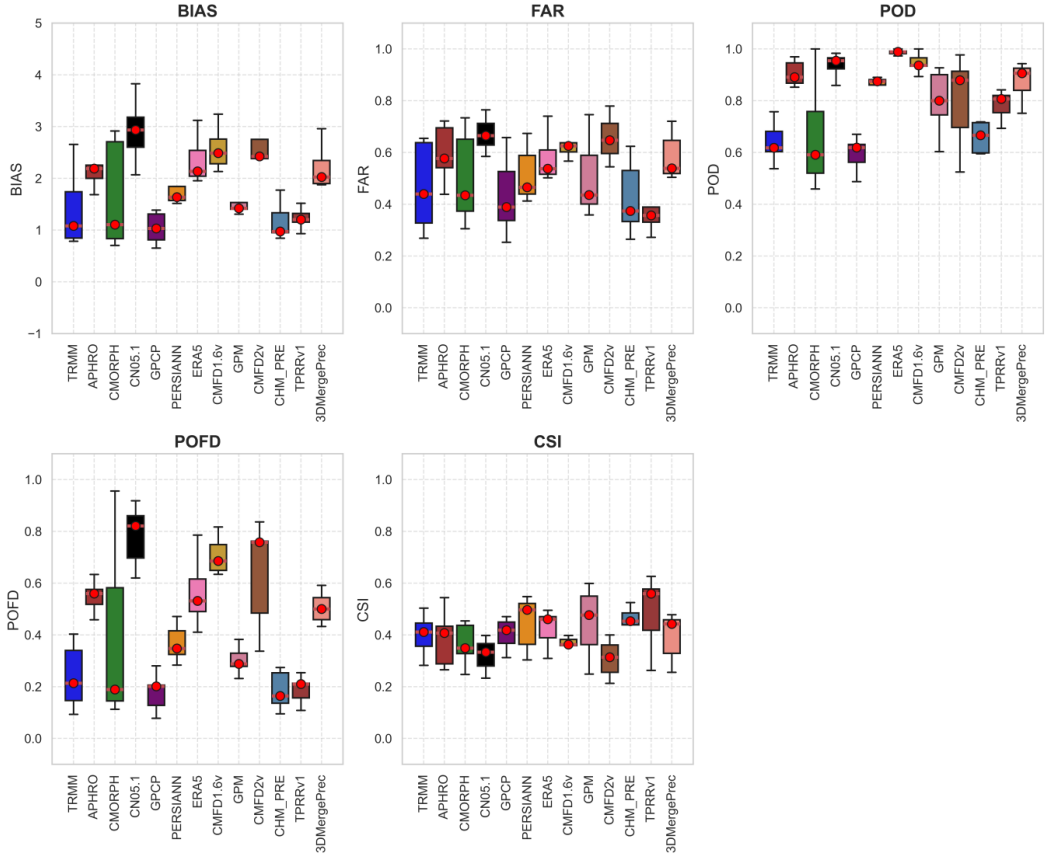

Fig 13 Statistical summary of precipitation event detection metrics evaluated against observation over the western TP. Each boxplot displays the interquartile range (25th – 75th percentiles), capturing the central 50% of station-level metric values. The red dot represents the median, and the whiskers extend to the minimum and maximum values, indicating the full spread of the data.

4.3 Performance for Extreme Precipitation Events

Although the probability distribution (Fig. 3) indicates that 3DM underestimates the probability of extreme precipitation events, this study further evaluates its capacity to capture such events. Extreme precipitation events are defined as those exceeding the 95th percentile threshold, calculated based on in-situ observations and uniformly applied

https://doi.org/10.5194/essd-2026-278
Preprint. Discussion started: 19 June 2026

across all datasets to ensure comparability. The number of extreme precipitation days is counted for each dataset, and the differences between estimated and observed values are presented in Fig. 14.

The 3DM, APHRO, CN05.1, and CMFD1.6v datasets generally exhibit negative deviations in extreme precipitation estimates, with pronounced spatial heterogeneity. Their estimated extreme precipitation days are approximately 4 days fewer than observations, primarily over the eastern Tibetan Plateau, while overestimations are observed over the northern plateau. This underestimation in the southern TP is consistent with the CDF characteristics shown in Fig. 3 and can be attributed to the model's limited sensitivity to extreme events. GPM, CMORPH, CHM_PRE, and ERA5 display moderate spatial variability, with differences generally ranging from −2 to 3.5 days, indicating a balanced but still uncertain capability in estimating extreme precipitation. In contrast, TRMM, CMFD2v, and TPRRv1 are characterized by overall positive deviations, with extreme precipitation days exceeding observations by more than 2 days, suggesting greater sensitivity to extreme events under the observed threshold. For GPCP and PERSIANN, a distinct spatial divide appears at approximately 22.5° N, with negative deviations to the north and positive deviations to the south. In the southern region, the number of extreme precipitation days exceeds observations by more than 5 days, which may be associated with regional climate characteristics and the adaptability of the models in this area.

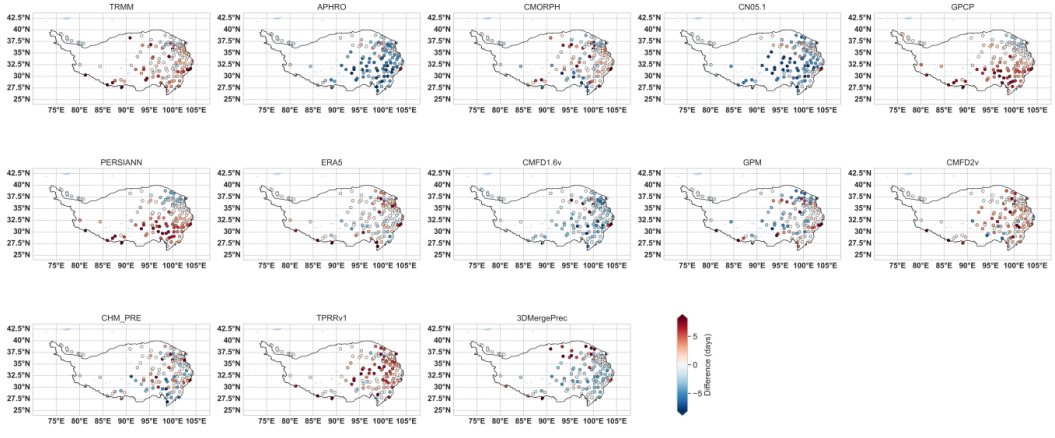

Fig 14 Spatial distribution of mean error between estimated and observed extreme precipitation days during 2001~2015

Figure 15 presents the spatial distribution of differences between estimated and observed extreme precipitation amounts during 2001 – 2015. The results indicate that 3DM exhibits good consistency with CMFD1.6v, CMFD2v, TPRRv1, and CHM_PRE, with no obvious bias detected at most stations. However, 3DM shows significant overestimation of extreme precipitation exceeding 5 mm at some stations in the northern region. This may be attributed to the region's specific

https://doi.org/10.5194/essd-2026-278
Preprint. Discussion started: 19 June 2026

Open Access Earth System Science Data Discussions

climatic and topographic conditions. For instance, the northern Tibetan Plateau is less influenced by monsoon activity, resulting in fewer extreme precipitation events; the model may therefore exhibit a systematic wet bias in this area. In contrast, APHRO, CN05.1, and ERA5 display negative biases at most stations, with extreme precipitation generally underestimated by more than 2 mm relative to observations. Meanwhile, TRMM, CMORPH, GPM, GPCP, and PERSIANN show widespread positive biases, with extreme precipitation overestimated by more than 4 mm at most stations. This suggests that these satellite-based and reanalysis products tend to overestimate extreme precipitation when evaluated against the observed threshold.

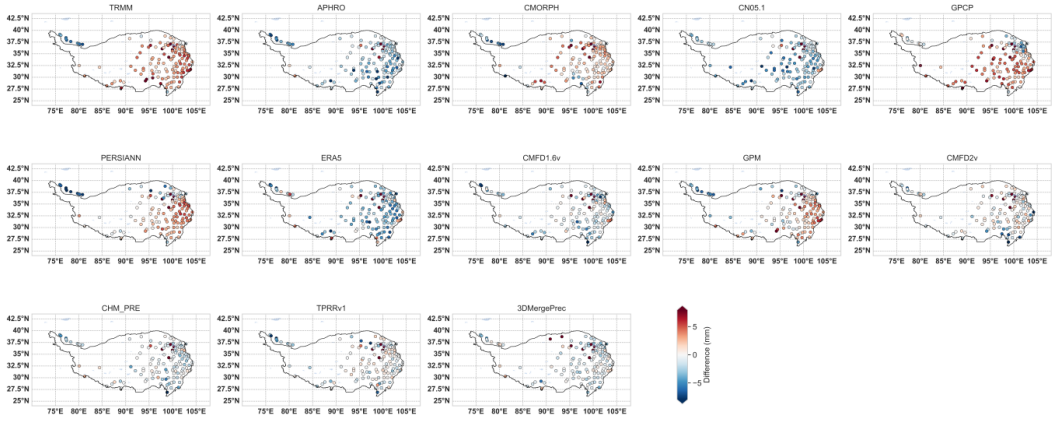

Fig 15 Spatial distribution of mean error between estimated and observed extreme precipitation amount during 2001~2015

To further assess the capability of each dataset in representing extreme precipitation trends, we calculate the ratio of the trend in estimated extreme precipitation days to that of observed days (dataset/observation), as shown in Fig. 16. The results indicate that the trend ratios for 3DM at most stations range from 0.5 to above 1.0, suggesting that 3DM can effectively capture the extreme precipitation trend over much of the Tibetan Plateau. However, in the southwestern plateau, the evaluation of extreme precipitation day trends remains highly uncertain due to the scarcity of in-situ observations, and most non-interpolated datasets fail to adequately reflect the observed trend. 3DM misestimates the trend of extreme precipitation days at some stations in the central, northern, and southwestern parts of the TP, which may be attributed to the insufficient representation of extreme events in the training samples.

The trend ratio for extreme precipitation amounts (Fig. 17) shows that 3DM is consistent with observations at most stations in the eastern plateau. However, similar to TRMM, CN05.1, PERSIANN, GPCP, and GPM, 3DM misestimates extreme precipitation trends over the central and western plateau. This suggests that the performance of the fusion product

https://doi.org/10.5194/essd-2026-278
Preprint. Discussion started: 19 June 2026

Open Access Earth System Science Data Discussions

may be constrained by limitations inherent in the multi-source precipitation fusion framework. Specifically, when integrating multiple datasets, the model may be influenced by the intrinsic characteristics of those datasets—such as their representativeness of extreme events—thereby propagating or amplifying existing biases.

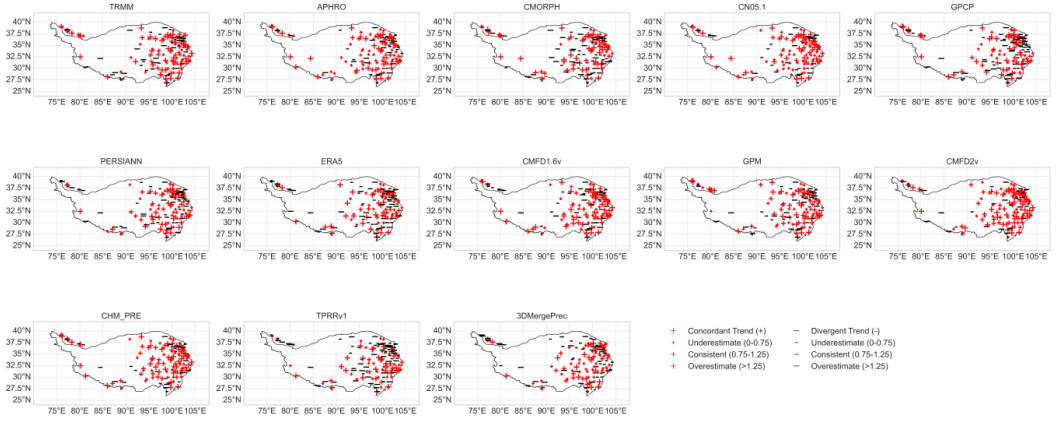

Fig 16 Distribution of the ratio between estimated and observed trends in extreme precipitation days during 2001~2015

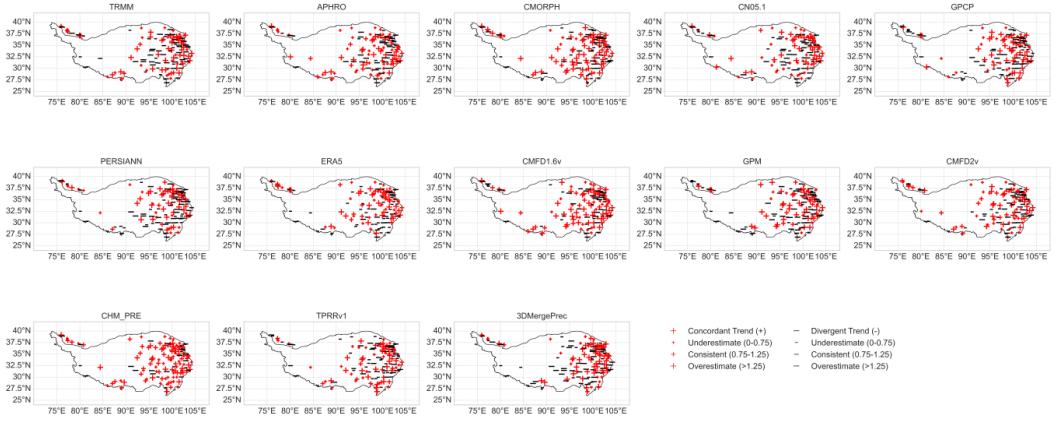

Fig 17 Distribution of the ratio between estimated and observed trends in extreme precipitation during 2001~2015

4. Discussion and Summary

4.1 Error Sources

The spatial pattern of errors in 3DM is primarily governed by three factors: the quality of input data, imbalanced training samples, and tail compression resulting from distribution transformation.

https://doi.org/10.5194/essd-2026-278
Preprint. Discussion started: 19 June 2026

First, satellite-based datasets are severely obstructed in regions with complex terrain—such as the Hengduan Mountains and the Yarlung Zangbo Grand Canyon—and their inherent errors are propagated into the fusion framework. Second, the 134 long-term observations used for training are predominantly concentrated in the eastern TP, with insufficient samples in western areas such as the Qiangtang and Hoh Xil regions. When driven solely by precipitation data and topography, the GAT model relies on features learned from the eastern region and the intrinsic characteristics of the input datasets to construct representations over the western TP, particularly in transitional zones. Although optimization has been achieved in the western region, errors arising from other sources remain unavoidable.

Finally, while the Gamma transformation effectively mitigates the issue of zero inflation, it simultaneously smooths the tail of the extreme precipitation distribution, leading to a systematic underestimation of precipitation events exceeding 20 mm. To address these limitations in future work, consideration could be given to employing Transfer Learning (TL) or Generative Adversarial Networks (GANs) to synthesize extreme precipitation samples, thereby expanding the tail of the training distribution. Additionally, incorporating more observations suitable for graph construction would help make the graph structure more representative of real-world conditions.

4.2 Graph Structure and Timeliness Extension

The current graph structure relies primarily on daily static adjacency, which is insufficient to capture the diurnal and intraseasonal variability of precipitation over the Tibetan Plateau. To address this limitation, future work could incorporate temporal dynamics into node state updates, enabling the construction of a dynamic spatiotemporal graph. Promising directions include hybrid architectures such as Spatiotemporal Graph Attention Networks (ST-GAT) or temporal Transformer-GNN models, which could improve subseasonal-to-seasonal precipitation estimation. Furthermore, graph nodes could be refined to higher spatial resolutions (10km or even 1 km)—by integrating multi-source covariates such as topographic aspect and vegetation indices. This would allow for exploration of the feasibility of high-resolution multi-source precipitation fusion, potentially yielding more detailed and accurate precipitation products.

4.3 Summary

To address the challenges of sparse and complex precipitation data over the Tibetan Plateau (TP), this study develops a multi-source fusion framework integrating Graph Attention Networks (GAT) with 3D-CNN. Using precipitation anomaly percentage as the training target—combined with logarithmic and Robust Z-Score normalization—alleviates the long-tail effect from Gamma-distributed precipitation. Transformer-enhanced GAT constructs spatial graphs to overcome local

https://doi.org/10.5194/essd-2026-278
Preprint. Discussion started: 19 June 2026

perspective limitations, while 3D-CNN captures local features, enabling effective global-local information coupling. The SWMSE loss function improves sensitivity to tail events.

Integrating 12 precipitation products through CDF-matching and dynamic weighting, we generate 3DM: a 0.25° daily merged precipitation dataset for the TP rainy season (1961–2021). This "preprocessing—feature fusion—post-processing" paradigm offers a technical reference for data fusion in complex regions. Evaluation results show: (1) Compared with satellite datasets (e.g., TRMM, GPM, CMORPH), 3DM reduces the mean squared error (MSE) at long-term stations by 30–40%, narrows high-error areas in the southeastern TP, and halves the number of stations with MSE >25 mm^2. For light precipitation (0.1–10 mm), 3DM slightly overestimates frequency but effectively corrects the underdetection bias common in satellite products, yielding a frequency distribution similar to observations. For extreme precipitation, although systematic underestimation persists due to tail smoothing, 3DM reasonably captures the spatial pattern over the eastern TP.

(2) Over the western TP, the RMSE of 3DM is 60–75% of that for satellite products. Mean MSE values are 10.78 mm^2 in the Changtang region and 17.09 mm^2 in the central-western TP, outperforming datasets such as CHM_PRE and CMFD2v. Unlike interpolation-based datasets, whose errors increase rapidly away from stations, 3DM achieves spatially balanced error distributions through graph-based information propagation. Precipitation trends derived from 3DM align closely with observations and pass more stringent significance tests, outperforming most long-term datasets in trend accuracy.

(3) However, certain limitations remain. Notable errors persist over the central Tibetan Plateau, along with an overestimation of light precipitation frequency and only modest improvements in precipitation event detection. These issues likely arise from the exclusive reliance on precipitation and topography as model inputs, with GAT graph construction based solely on spatial relationships. Complex precipitation processes influenced by dynamic atmospheric conditions may be obscured by inconsistencies among input datasets, highlighting the need to incorporate dynamic constraints in future work. Overall, despite limitations such as tail compression in extreme precipitation and sparse samples over the western plateau, 3DM demonstrates clear improvements in precipitation magnitude estimation, trend characterization, and event detection across the western TP. Future work will focus on enhancing the dataset's accuracy and applicability through sample augmentation, dynamic graph construction, and high-resolution downscaling. A rolling update scheme is also planned to ensure the dataset remains timely and relevant for long-term use.

https://doi.org/10.5194/essd-2026-278
Preprint. Discussion started: 19 June 2026

Open Access Earth System Science Data Discussions

Data availability

All datasets used for multi-source fusion are openly accessible. CMORPH, TRMM, GPCP can be downloaded at https://ncar.ucar.edu/. APHRODITE (APHRO) can be downloaded at http://aphrodite.st.hirosaki-u.ac.jp/download/. CN05.1 can be downloaded at http://data.cma.cn/. TPRRv1, CMFD1.6v, CMFD2v can be downloaded at https://data.tpdc.ac.cn/. ERA5 can be downloaded at https://cds.climate.copernicus.eu/datasets/derived-era5-single-levels-daily-statistics?tab=overview. CHM_PREv1 can be downloaded at https://doi.org/10.6084/m9.figshare.21432123.v4. GPM can be downloaded at https://disc.gsfc.nasa.gov/datasets?keywords=GPM. PERSIANN can be downloaded at https://www.ncei.noaa.gov/. The plateau boundary is defined based on the Integration dataset of Tibet Plateau boundary, which can be downloaded at https://doi.org/10.11888/Geogra.tpdc.270099. ASTER GDEM can be downloaded at https://search.earthdata.nasa.gov/. This fusion dataset can available at https://doi.org/10.11888/Atmos.tpdc.303443, and includes daily precipitation during the rainy season (June–September) from 1961 to 2021, with a spatial resolution of 0.25°.

Author contributions

Zuo Wen：Conceptualization, data curation, formal analysis, investigation, methodology, project administration, software, validation, visualization, writing – original draft, writing – review & editing.

Baiquan Zhou: Conceptualization, funding acquisition, investigation, methodology, project administration, resources, supervision, writing – review & editing.

Panmao Zhai: Conceptualization, methodology, supervision, writing – review & editing.

Competing interests

The authors declare that they have no conflict of interest.

Financial support

This study was supported by the second Tibetan Plateau Scientific Expedition Research Program (Grant No.2022QZKK0101).

References

Andermann, C., Bonnet, S., and Gloaguen, R. (2011) Evaluation of precipitation data sets along the Himalayan front:

https://doi.org/10.5194/essd-2026-278
Preprint. Discussion started: 19 June 2026

627 PRECIPITATION EVALUATION. *Geochemistry, Geophysics, Geosystems* 12(7): n/a-n/a.

628 Arulraj, M., and Barros, A. P. (2019) Improving quantitative precipitation estimates in mountainous regions by modelling
629 low-level seeder-feeder interactions constrained by Global Precipitation Measurement Dual-frequency Precipitation Radar
630 measurements. *Remote Sensing of Environment* 231: 111213.

631 Baudouin, J.-P., Herzog, M., and Petrie, C. A. (2020) Cross-validating precipitation datasets in the Indus River basin.
632 *Hydrology and Earth System Sciences* 24(1): 427–450.

633 Beck, H. E., Vergopolan, N., Pan, M., Levizzani, V., Van Dijk, A. I. J. M., Weedon, G. P., Brocca, L., Pappenberger, F.,
634 Huffman, G. J., and Wood, E. F. (2017) Global-scale evaluation of 22 precipitation datasets using gauge observations and
635 hydrological modeling. *Hydrology and Earth System Sciences* 21(12): 6201–6217.

636 Bhardwaj, A., Ziegler, A. D., Wasson, R. J., and Chow, W. T. L. (2017) Accuracy of rainfall estimates at high altitude in
637 the Garhwal Himalaya (India): A comparison of secondary precipitation products and station rainfall measurements.
638 *Atmospheric Research* 188: 30–38.

639 Bharti, V., and Singh, C. (2015) Evaluation of error in TRMM 3B42V7 precipitation estimates over the Himalayan region.
640 *Journal of Geophysical Research: Atmospheres* 120(24): 12458–12473.

641 Bhatt, B. C., Sobolowski, S., and King, M. P. (2014) Assessment of downscaled current and future projections of diurnal
642 rainfall patterns for the Himalaya. *Journal of Geophysical Research: Atmospheres* 119(22).

643 Chen, S., Hong, Y., Cao, Q., Gourley, J. J., Kirstetter, P., Yong, B., Tian, Y., Zhang, Z., Shen, Y., Hu, J., and Hardy, J. (2013)
644 Similarity and difference of the two successive V6 and V7 TRMM multisatellite precipitation analysis performance over
645 China. *Journal of Geophysical Research: Atmospheres* 118(23).

646 Chen, W., Liu, Y., Zhang, G., Yang, K., Zhou, T., Wang, J., and Shum, C. K. (2022) What Controls Lake Contraction and
647 Then Expansion in Tibetan Plateau's Endorheic Basin Over the Past Half Century? *Geophysical Research Letters* 49(20):

https://doi.org/10.5194/essd-2026-278
Preprint. Discussion started: 19 June 2026

e2022GL101200.

Cheng, Y., Zhang, X., Wang, K., Zhang, Y., Guo, Y., and Shen, Y.-J. (2025) Multidimensional evaluation of satellite-based and reanalysis-based precipitation datasets in the Tibetan Plateau. *Journal of Hydrology* 660: 133364.

Di, Z., Duan, Q., Gong, W., Wang, C., Gan, Y., Quan, J., Li, J., Miao, C., Ye, A., and Tong, C. (2015) Assessing WRF model parameter sensitivity: A case study with 5 day summer precipitation forecasting in the Greater Beijing Area. *Geophysical Research Letters* 42(2): 579–587.

Du, Y., Wang, D., Zhu, J., Lin, Z., and Zhong, Y. (2022) Intercomparison of multiple high-resolution precipitation products over China: Climatology and extremes. *Atmospheric Research* 278: 106342.

Duncan, J. M. A., and Biggs, E. M. (2012) Assessing the accuracy and applied use of satellite-derived precipitation estimates over Nepal. *Applied Geography* 34: 626–638.

Gavahi, K., Foroumandi, E., and Moradkhani, H. (2023) A deep learning-based framework for multi-source precipitation fusion. *Remote Sensing of Environment* 295: 113723.

Gebregiorgis, A. S., and Hossain, F. (2015) How well can we estimate error variance of satellite precipitation data around the world? *Atmospheric Research* 154: 39–59.

Hamza, A., Anjum, M. N., Masud Cheema, M. J., Chen, X., Afzal, A., Azam, M., Kamran Shafi, M., and Gulakhmadov, A. (2020) Assessment of IMERG-V06, TRMM-3B42V7, SM2RAIN-ASCAT, and PERSIANN-CDR Precipitation Products over the Hindu Kush Mountains of Pakistan, South Asia. *Remote Sensing* 12(23): 3871.

Hochreiter, S., and Schmidhuber, J. (1997) Long Short-Term Memory. *Neural Computation* 9(8): 1735–1780.

Huffman, G. J., Adler, R. F., Bolvin, D. T., and Nelkin, E. J. (2010) The TRMM Multi-Satellite Precipitation Analysis (TMPA). In Gebremichael, M. and Hossain, F. (Eds), *Satellite Rainfall Applications for Surface Hydrology*. Dordrecht: Springer Netherlands doi:10.1007/978-90-481-2915-7_1.

https://doi.org/10.5194/essd-2026-278
Preprint. Discussion started: 19 June 2026

669 Jena, P., Garg, S., and Azad, S. (2020) Performance Analysis of IMD High-Resolution Gridded Rainfall (0.25° × 0.25°)
670 and Satellite Estimates for Detecting Cloudburst Events over the Northwest Himalayas. *Journal of Hydrometeorology* 21(7):
671 1549–1569.
672 Jiang, Y., Yang, K., Shao, C., Zhou, X., Zhao, L., Chen, Y., and Wu, H. (2021) A downscaling approach for constructing
673 high-resolution precipitation dataset over the Tibetan Plateau from ERA5 reanalysis. *Atmospheric Research* 256: 105574.
674 Khandu, Awange, J. L., and Forootan, E. (2016) An evaluation of high-resolution gridded precipitation products over
675 Bhutan (1998–2012). *International Journal of Climatology* 36(3): 1067–1087.
676 Kumar, M., Hodnebrog, Ø., Sophie Daloz, A., Sen, S., Badiger, S., and Krishnaswamy, J. (2021) Measuring precipitation
677 in Eastern Himalaya: Ground validation of eleven satellite, model and gauge interpolated gridded products. *Journal of*
678 *Hydrology* 599: 126252.
679 Li, G., Chen, H., Xu, M., Zhao, C., Zhong, L., Li, R., Fu, Y., and Gao, Y. (2022) Impacts of Topographic Complexity on
680 Modeling Moisture Transport and Precipitation over the Tibetan Plateau in Summer. *Advances in Atmospheric Sciences*
681 39(7): 1151–1166.
682 Li, H., Haugen, J. E., and Xu, C.-Y. (2018) Precipitation pattern in the Western Himalayas revealed by four datasets.
683 *Hydrology and Earth System Sciences* 22(10): 5097–5110.
684 Liu, H., Yang, Q., Liu, Z., Shao, J., and Wang, G. (2024) An attention-mechanism-based deep fusion model for improving
685 quantitative precipitation estimation in a sparsely-gauged basin. *Journal of Hydrology* 628: 130568.
686 Lyu, Y., Yong, B., Huang, F., Qi, W., Tian, F., Wang, G., and Zhang, J. (2024) Investigating twelve mainstream global
687 precipitation datasets: Which one performs better on the Tibetan Plateau? *Journal of Hydrology* 633: 130947.
688 Ma, Y., Yang, Y., Han, Z., Tang, G., Maguire, L., Chu, Z., and Hong, Y. (2018) Comprehensive evaluation of Ensemble
689 Multi-Satellite Precipitation Dataset using the Dynamic Bayesian Model Averaging scheme over the Tibetan plateau.

https://doi.org/10.5194/essd-2026-278
Preprint. Discussion started: 19 June 2026

690 *Journal of Hydrology* 556: 634–644.

691 Maggioni, V., Nikolopoulos, E. I., Anagnostou, E. N., and Borga, M. (2017) Modeling Satellite Precipitation Errors Over
692 Mountainous Terrain: The Influence of Gauge Density, Seasonality, and Temporal Resolution. *IEEE Transactions on*
693 *Geoscience and Remote Sensing* 55(7): 4130–4140.

694 Ménégoz, M., Gallée, H., and Jacobi, H. W. (2013) Precipitation and snow cover in the Himalaya: from reanalysis to
695 regional climate simulations. *Hydrology and Earth System Sciences* 17(10): 3921–3936.

696 Miao, C., Immerzeel, W. W., Xu, B., Yang, K., Duan, Q., and Li, X. (2024) Understanding the Asian water tower requires
697 a redesigned precipitation observation strategy. *Proceedings of the National Academy of Sciences* 121(23): e2403557121.

698 Oliveira, R., Maggioni, V., Vila, D., and Morales, C. (2016) Characteristics and Diurnal Cycle of GPM Rainfall Estimates
699 over the Central Amazon Region. *Remote Sensing* 8(7): 544.

700 Qiu, J. (2014) Tibetan plateau gets wired up for monsoon prediction. *Nature* 514(7520): 16–17.

701 Ren, Z., Yu, Y., Zou, F.X., Xu, Y. (2012) Quality Detection of Surface Historical Basic Meteorological Data. Journal of
702 Applied Meteorological Science 23, 739–747. https://doi.org/10.3969/j.issn.1001-7313.2012.06.011 (in Chinese)

703 Shah, H. L., and Mishra, V. (2016) Uncertainty and Bias in Satellite-Based Precipitation Estimates over Indian
704 Subcontinental Basins: Implications for Real-Time Streamflow Simulation and Flood Prediction*. *Journal of*
705 *Hydrometeorology* 17(2): 615–636.

706 Shi, X., Chen, Z., Wang, H., Yeung, D.-Y., Wong, W., and Woo, W. (2015/19/September) Convolutional LSTM Network:
707 A Machine Learning Approach for Precipitation Nowcasting. arXiv doi:10.48550/arXiv.1506.04214.

708 Silva, V. B. S., Kousky, V. E., and Higgins, R. W. (2011) Daily Precipitation Statistics for South America: An
709 Intercomparison between NCEP Reanalyses and Observations. *Journal of Hydrometeorology* 12(1): 101–117.

710 Tong, K., Su, F., Yang, D., Zhang, L., and Hao, Z. (2014) Tibetan Plateau precipitation as depicted by gauge observations,
711 reanalyses and satellite retrievals. *International Journal of Climatology* 34(2): 265–285.

https://doi.org/10.5194/essd-2026-278
Preprint. Discussion started: 19 June 2026

712 Vaswani, A., Shazeer, N., Parmar, N., Uszkoreit, J., Jones, L., Gomez, A. N., Kaiser, L., and Polosukhin, I. (2017/2/August)
713 Attention Is All You Need. arXiv doi:10.48550/arXiv.1706.03762.
714 Vatamány, L., and Mehrkanoon, S. (2025) Graph Dual-stream Convolutional Attention Fusion for precipitation nowcasting.
715 *Engineering Applications of Artificial Intelligence* 141: 109788.
716 Veličković, P., Cucurull, G., Casanova, A., Romero, A., Liò, P., and Bengio, Y. (2018/4/February) Graph Attention
717 Networks. arXiv doi:10.48550/arXiv.1710.10903.
718 Wu, H., Yang, Q., Liu, J., and Wang, G. (2020) A spatiotemporal deep fusion model for merging satellite and gauge
719 precipitation in China. *Journal of Hydrology* 584: 124664.
720 Wu, X., Su, J., Ren, W., Lü, H., and Yuan, F. (2023) Statistical comparison and hydrological utility evaluation of ERA5-
721 Land and IMERG precipitation products on the Tibetan Plateau. *Journal of Hydrology* 620: 129384.
722 Yan, W., Liu, S., Zou, Y., Liu, X., Wen, D., Hu, Y., Yang, D., Xie, J., and Zhao, L. (2025) Convolutional Graph Neural
723 Network with Novel Loss Strategies for Daily Temperature and Precipitation Statistical Downscaling over South China.
724 *Advances in Atmospheric Sciences* 42(1): 232–247.
725 Yan, Y., You, Q., Wu, F., Pepin, N., and Kang, S. (2020) Surface mean temperature from the observational stations and
726 multiple reanalyses over the Tibetan Plateau. *Climate Dynamics* 55(9–10): 2405–2419.
727 Yao, F., Wang, J., Yang, K., Wang, C., Walter, B. A., and Crétaux, J.-F. (2018) Lake storage variation on the endorheic
728 Tibetan Plateau and its attribution to climate change since the new millennium. *Environmental Research Letters* 13(6):
729 064011.
730 Yao, T., Xue, Y., Chen, D., Chen, F., Thompson, L., Cui, P., et al. (2019) Recent Third Pole's Rapid Warming Accompanies
731 Cryospheric Melt and Water Cycle Intensification and Interactions between Monsoon and Environment: Multidisciplinary
732 Approach with Observations, Modeling, and Analysis. *Bulletin of the American Meteorological Society* 100(3): 423–444.

https://doi.org/10.5194/essd-2026-278
Preprint. Discussion started: 19 June 2026

733 Yatagai, A., Kamiguchi, K., Arakawa, O., Hamada, A., Yasutomi, N., and Kitoh, A. (2012) APHRODITE: Constructing a
734 Long-Term Daily Gridded Precipitation Dataset for Asia Based on a Dense Network of Rain Gauges. *Bulletin of the*
735 *American Meteorological Society* 93(9): 1401–1415.
736 You, Q., Kang, S., Li, J., Chen, D., Panmao Zhai, and Ji, Z. (2021) Several research frontiers of climate change over the
737 Tibetan Plateau. *Journal of Glaciology and Geocryology* 43(3): 885–901.
738 Yousaf, U., De Rango, A., Furnari, L., D'Ambrosio, D., Senatore, A., and Mendicino, G. (2025) Spatio-temporal graph
739 neural networks to improve precipitation forecasts from numerical models. *Soft Computing* 29(9–10): 4481–4494.
740 Yuan, X., Yang, K., Lu, H., He, J., Sun, J., and Wang, Y. (2021) Characterizing the features of precipitation for the Tibetan
741 Plateau among four gridded datasets: Detection accuracy and spatio-temporal variabilities. *Atmospheric Research* 264:
742 105875.
743 Zhang, L., Li, X., Zheng, D., Zhang, K., Ma, Q., Zhao, Y., and Ge, Y. (2021) Merging multiple satellite-based precipitation
744 products and gauge observations using a novel double machine learning approach. *Journal of Hydrology* 594: 125969.
745